



## **Initial Geometric Imperfection Measurement and Characterization of Cold-Formed Steel C-Section Structural Members with 3D Non-Contact Measurement Techniques**

L.E. McAnallen<sup>1</sup>, D.A. Padilla-Llano<sup>2</sup>, X. Zhao<sup>3</sup>, C.D. Moen<sup>4</sup>, B.W. Schafer<sup>5</sup>, M.R. Eatherton<sup>6</sup>

### **Abstract**

Local flange and web imperfections, cross-sectional twist, and global sweep were measured for cold-formed steel C-section structural members (studs and joists) using non-contact measurement methods (photogrammetry and laser scanning) and a manual measurement method (dial gauges mounted on a precision rail). Cold-formed steel members acquire geometric imperfections from manufacturing, shipping, storage and construction, and these imperfections affect axial and flexural capacity. Photogrammetry and a newly constructed laser measurement method are demonstrated to be viable and accurate alternatives to manual measurements, producing 3D point clouds that allow detailed study of imperfections along a member. Measured imperfections provide an accurate geometry representation, which can be used in experimental comparisons and computational modeling. Each measured imperfection shape is characterized as a series of trigonometric functions along the member's length. This format allows researchers to reconstruct the member geometry and to understand the influence of imperfection shape on local, distortional, and global buckling deformations. The imperfection fields measured in this study, as well as past measurements from previous research, are organized with a common format in a new imperfections database hosted by the Cold-Formed Steel Research Consortium for communal access and future study.

### **1. Introduction**

This paper explores 3D non-contact methods for measuring initial geometric imperfection fields in cold-formed steel (CFS) lipped C-section joists and studs. Thin-walled CFS structural member cross-sectional dimensions are much larger than their base metal thickness, which makes their load-deformation response sensitive to initial geometric imperfections. Stiffness and ultimate strength tend to decrease when imperfections are present (Godoy 1996; Schafer et al., 2010) either as local imperfections caused by shipping and handling or global imperfections along the length,

---

<sup>1</sup> Graduate Research Assistant, Civil & Environmental Engineering, Virginia Tech, <lem421@vt.edu>

<sup>2</sup> Graduate Research Assistant, Civil & Environmental Engineering, Virginia Tech, <dapadill@vt.edu>

<sup>3</sup> Graduate Research Assistant, Dept. of Civil Engineering, Johns Hopkins University, <xzhao16@jhu.edu>

<sup>4</sup> Associate Professor, Civil & Environmental Engineering, Virginia Tech, <cmoen@vt.edu>

<sup>5</sup> Professor, Dept. of Civil Engineering, Johns Hopkins University, <schafer@jhu.edu>

<sup>6</sup> Assistant Professor, Civil & Environmental Engineering, Virginia Tech, <meather@vt.edu>

e.g., sweep caused from sheet coiling (Zeinoddini 2011; Moen et al., 2008; Quach et al., 2004). A first step, and the focus of this paper, is to define and validate a procedural framework for accurately measuring, characterizing, and organizing 3D imperfection fields.

The most frequently used method to characterize global imperfections considers a maximum imperfection amplitude (e.g.,  $L/960$  for sweep in ASTM C955-09). The method typically used to characterize cross-sectional imperfections considers two types: local web ( $d_1$ ) and local flange ( $d_2$ ) imperfections, as shown in Fig. 1 (e.g., Schafer and Peköz 1998). This method uses probability density functions of occurrence for a specific imperfection magnitude to set as the maximum imperfection amplitude (proportional to member thickness) and using cross-sectional buckling modes to distribute it along the member. The probability density functions were derived from single point hand measurements of imperfections along a member length. This probabilistic approach is still applicable for 3D imperfection fields. However, updated methods for using imperfection shapes and magnitudes in computational simulations are needed as 3D data fields are collected.

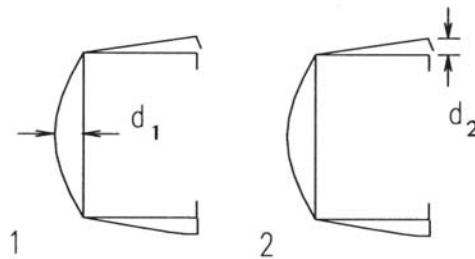


Figure 1: Imperfections defined by Schafer and Peköz (1998).

Recent work is beginning to hash out these new recommendations, starting with a comprehensive U.S. imperfection measurement study of 210 CFS specimens (Zeinoddini 2011) that also collected and summarized existing imperfection measurements from previous studies, including full-field measurements on channel sections (Rasmussen and Hancock 1988; Young and Rasmussen 1999; Peterman 2012). Spectral approaches for representing imperfections now exist for combinations of buckling modes (Zeinoddini and Schafer 2012). The work presented in this paper expands on these ideas with a simple procedure that uses a generalized sum of sine-waves  $\delta$  to describe magnitude imperfection variations along the length and that are imposed by directly modifying the member cross section geometry through simple transformations.

This paper begins by describing two non-contact measurement methods for taking 3D imperfections measurements, photogrammetry and laser scanning. These methods are used to study imperfections in a group of CFS members, and the data fields are compared to well-established manual measurement techniques. Maximum imperfection magnitudes are computed for each specimen and compared to ASTM imperfection tolerances. Measurement error for each of the non-contact measurement methods is quantified. The 3D measurement data is formatted and input into a new imperfections database hosted and maintained by the Cold-Formed Steel Research Consortium ([www.cfsrc.org](http://www.cfsrc.org)).

## 2. Imperfection Measurement Methods

The imperfection measurement methods and procedures employed in this study: photogrammetry, laser scanning, and the manual method (dial gauges mounted on a precision rail), are introduced in the following subsections.

### 2.1 Photogrammetry

In the photogrammetry method, a CFS member is covered with unique, recognizable targets strategically placed to capture its geometry. Sets of photos are taken from multiple viewpoints around the specimen, and then processed using commercial software PhotoModeler (Eos 2012), to identify all the targets. A gradient based optimization algorithm built into PhotoModeler approximates the target locations in 3D by finding the target coordinates that minimize the square of the difference between  $x$ - $y$ - $z$  coordinates at each camera location for each photo. The final product is a 3D point cloud, where each point corresponds to a target.

Ringed automatically detected (RAD) targets and plain dot targets are used in this study (Fig. 2a, and Fig. 2b). RAD targets are unique markers, each with a different pattern that allows automated photo processing with PhotoModeler. Unlike RAD targets, all dot targets are identical. Both targets can be scaled to fit within member dimensions.

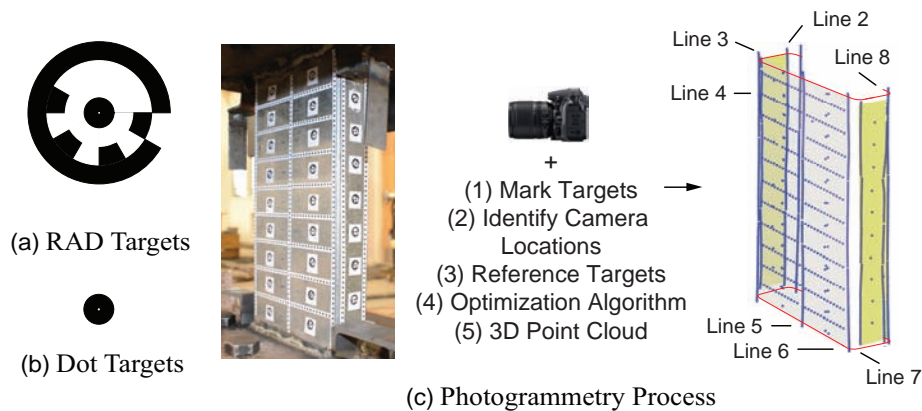


Figure 2: (a) RAD targets and (b) dot targets are used to (c) complete the photogrammetry process of marking targets, identifying camera locations, referencing targets, and using an optimization algorithm to process a 3D point cloud.

On each specimen, RAD targets were affixed along the web and flanges at equal spacing. The dot targets were placed in longitudinal lines, representing lines 2 through 8 in Fig. 2c. A Nikon D7000 high-resolution DSLR (digital single-lens reflex) camera was used to take photographs of each target-covered member from different angles and positions along the member's length. The following photogrammetry parameters were used to obtain optimum accuracy in PhotoModeler: each photo set should contain (i) photos with at least 50% point coverage, (ii) at least 50% point overlap between photos, (iii) at least 10 RAD targets in each photo, and (iv) a camera station angle separation between  $30^\circ$  and  $90^\circ$  for most photos. The 3D point cloud is used to obtain local and global imperfection shapes and magnitudes relative to a perfect reference specimen as described later in Section 3.

## 2.2 Laser Scanning

The laser scanning method utilizes triangulation techniques through a solid-state light/detector sensor to achieve the non-contact measurement target. A laser beam is projected on the targeted specimen and a portion of the beam is reflected through focusing optics onto a detector. The detected signal is used to determine the relative distance to the target. The laser sensor LJ-V7300 used in the Thin-Walled Structures Lab at Johns Hopkins University, employs 800 blue-light laser points to provide a 2D profile up to 304 mm wide. The CFS member is placed onto the supported beam and below the laser sensor. The surface of interest is facing up to the laser scanner (Fig. 3). The laser head is able to profile the target in frequencies up to 16 kHz. This property allows the laser sensor to scan the specimen longitudinally using an automated linear drive system mounted as part of the measurement rig, and obtain a 3D profile of the surface of interest.

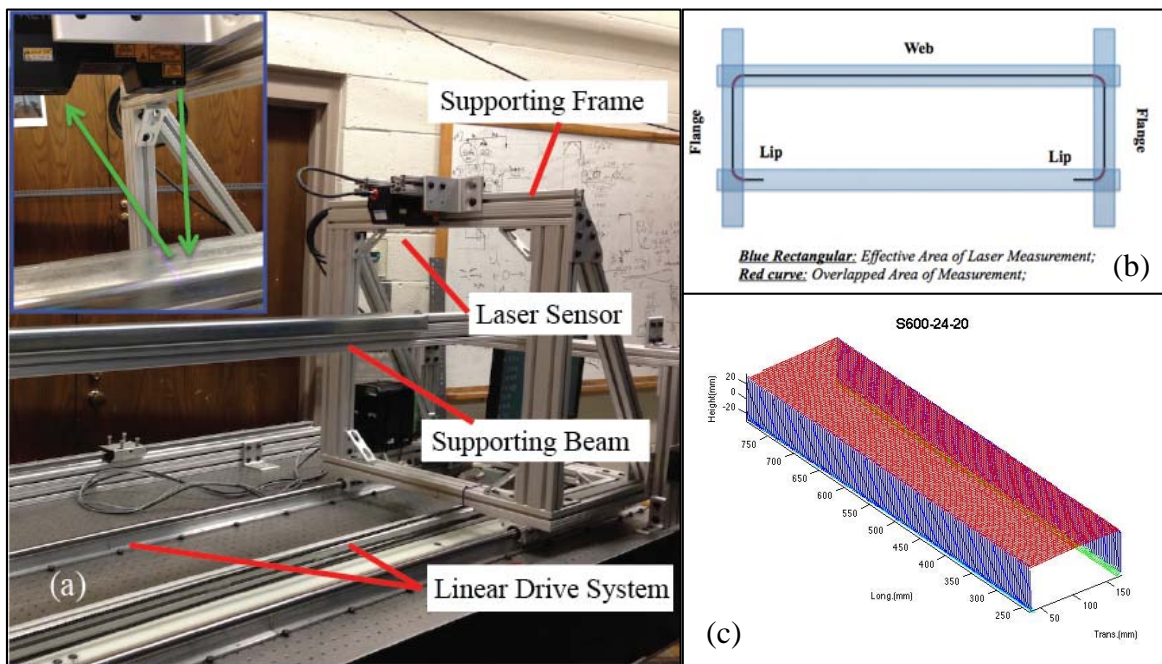


Figure 3: Laser scanning setup (a), model stitching scheme (b), and reconstructed 3D point cloud (c).

Four sides, i.e. web, right flange, left flange and lips, of the specimen are scanned including extra length beyond the two ends to include part of the supporting beam (Fig. 3a). One additional scan of the supporting beam alone is required to pair the four scanned surfaces which is used as a reference for orientation and reconstruction of the 3D point cloud (Fig. 3c). The four effective measurement areas of the laser scanner (Fig. 3b) overlap at the corners of the section and are paired up using a nonlinear least square approach. Large point clouds obtained using the laser scanning method allow precise calculation of member local and global imperfections.

## 2.3 Manual Measurement Method (dial gauges mounted on precision rail)

The manual measurement method involves recording readings from three dial gages mounted to a carriage riding on a high-precision aluminum rail along the member's length as depicted in Fig. 4. Imperfections are manually measured at three locations across the web, corresponding to lines 4, 5, and 6 in Fig. 3, at 25 mm, 51 mm, or 152 mm longitudinal increments, for member lengths of  $L=305\text{mm}$ ,  $610\text{mm}$  and  $L \geq 2286\text{mm}$  respectively. Dial gauge measurements were used to obtain

global and local web imperfection shapes and magnitudes. Flange imperfections in the manual measurement method were derived from measured cross-section dimensions.

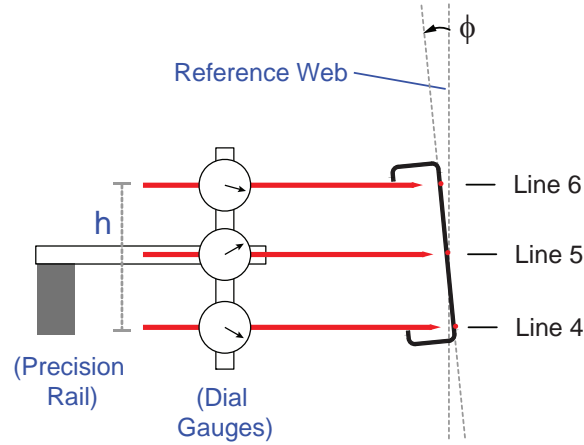


Figure 4: Dial gage and precision rail setup for manual measurements.

Although the procedures to obtain a 3D point cloud that represents the geometry of a CFS member are different for each method, the procedures in the following section are common to the three methods for deriving global and cross-sectional imperfection measurements of the C-shaped members in this study.

### 3. Measurement Notation and Definitions

Initial geometric imperfections are defined as the measured geometry deviations from a perfect reference member. A perfect member is straight and has a perfect C-shaped cross-section. The *perfect C-shaped cross-section* has a flat web surface, flat flanges perpendicular to the web, and dimensions corresponding to measured values at each member mid-length as shown Fig. 5a. Five imperfection quantities named: out-of-straightness in the weak axis ( $\delta_B$ ), out-of-straightness in the strong axis ( $\delta_C$ ), twist ( $\phi$ ), web local buckling ( $\delta_W$ ), and flange imperfections ( $\delta_{FE}$  and  $\delta_{FW}$ ) are characterized herein, see Fig. 5. Longitudinal lines extending the length of the measured member and located as shown in Fig. 5a are used in this study to compute local imperfections pertinent to CFS channel sections. Lines 2-4 and 6-8 are located at the edges of the corresponding flat portions of the cross-section, such that points on these lines do not fall on the cross-section's rounded corners. Line 5 is located at the center of the measured web height. In the photogrammetry method, dot targets (Fig. 2b) were placed along these lines making sure they laid flat to directly obtain the needed coordinates.

The orientation of the measured 3D point cloud is defined by first finding the principal axes of the point cloud. To find the principal axes an orthogonal least squared approach is used to determine the 3D line that best fits the point cloud and two orthogonal vectors that will complete the reference coordinate system. The principal component analysis, PCA (Jolliffe 2002) was used in this study to find these principal axes, however, more complex procedures could also be used (e.g. Liu and Ramani 2009). For a prismatic member without imperfections (e.g., channel) the PCA procedure gives the direction vector of the 3D line aligned with the longitudinal axis, the direction of the major cross-section axis and the direction of the minor cross-section axis. In a member with

imperfections, the 3D line that best fits the point cloud should align with the longer dimension, thus the length  $L$  of the member, and it will be regarded herein as the *reference axis*. The 3D point cloud is rotated such that the *reference axis* is vertical, aligning with the  $z$ -axis and the two orthogonal vectors align with the  $x$ - and  $y$ - axes respectively.

### 3.1 Global Imperfections

Global imperfections, i.e., out-of-straightness and twist, are defined, after orienting the member, respect to a *centroidal axis* of the member that is determined as follows. Cross sections are sampled for different  $z$ -coordinates along the *reference axis*, their centroid is found as well as the cross-section principal axes (using the PCA for example). The centroid of all sampled cross sections defines the *centroidal axis* and the centroid of this centroidal axis defines the *center point* needed to derive global sweep imperfections. The principal axes are used to obtain initial twist imperfections. Out-of-straightness in the weak axis direction,  $\delta_B$ , (see Fig. 5b), at a specific  $z$ -coordinate along the length, is the distance parallel to the  $y$ - axis between points in the *centroidal axis* to the *center point*. Similarly, out-of-straightness in the strong axis direction,  $\delta_C$ , at a certain  $z$ -coordinate along the length is the distance parallel to the  $x$ - axis between points in the *centroidal axis* to the *center point* (see Fig. 5b). The cross-section initial twist,  $\phi$  at a specific  $z$ -coordinate along the length is the angle between the major principal axes (found using PCA or other methods), and the  $x$ -axis, as shown in Fig. 5c.

### 3.2 Cross-sectional Imperfections

Local imperfections, i.e., local web and flange imperfections, are defined respect to a *perfect C-shaped cross-section* that rides along the member that has global imperfections. Such *perfect C-shaped cross-section* is defined using measured dimensions. The web imperfection magnitude,  $\delta_W$ , at any  $z$ -coordinate along the member is the perpendicular distance from a point in line 5 to the web of the *perfect C-shaped cross-section*, i.e., the line connecting points in lines 4 and 6 (see Fig. 5d). The flange east and west imperfections,  $\delta_{FE}$  and  $\delta_{FW}$ , are computed as the perpendicular distances of points in lines 2 and 8 to the corresponding flanges of the *perfect C-shaped cross-section*, as shown in Fig. 5d.

This imperfection reference system and notation described above are employed in the next section for a non-contact measurement study on a group of CFS members.

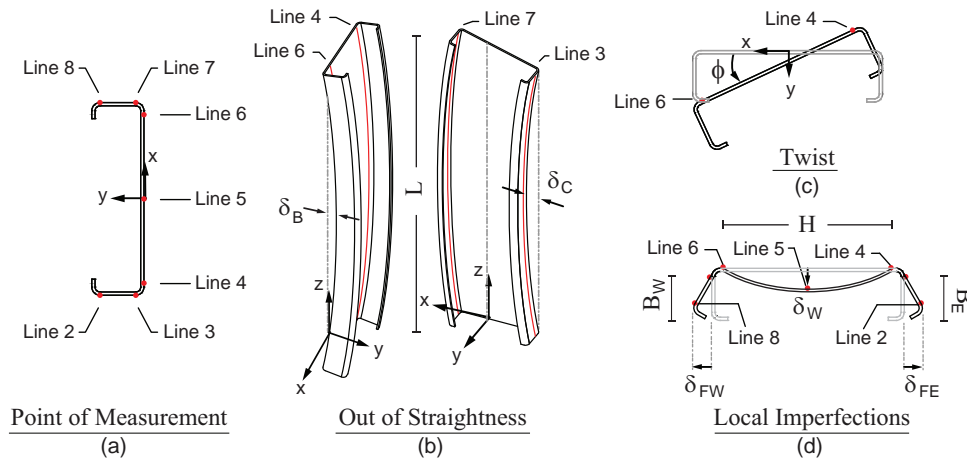


Figure 5: Global and Local Imperfection Definitions

#### 4. Imperfection Measurement Study using Photogrammetry

Photogrammetry and the manual measurement methods (dial gauges and precision rail), described in Section 2, were used to measure initial imperfections for 20 CFS members with lengths ranging from  $L=305\text{mm}$  to  $3048\text{mm}$ . These specimens were recently tested under cyclic and monotonic loading to characterize cyclic behavior and quantify energy dissipation of axial and flexural CFS members for the American Iron and Steel Institute (AISI) (Padilla-Llano et al. 2013). The specimen naming convention linking this imperfection study to the multi-year AISI project is described in Fig. 6 and measured cross-section dimensions are summarized in the Appendix, Table A1.

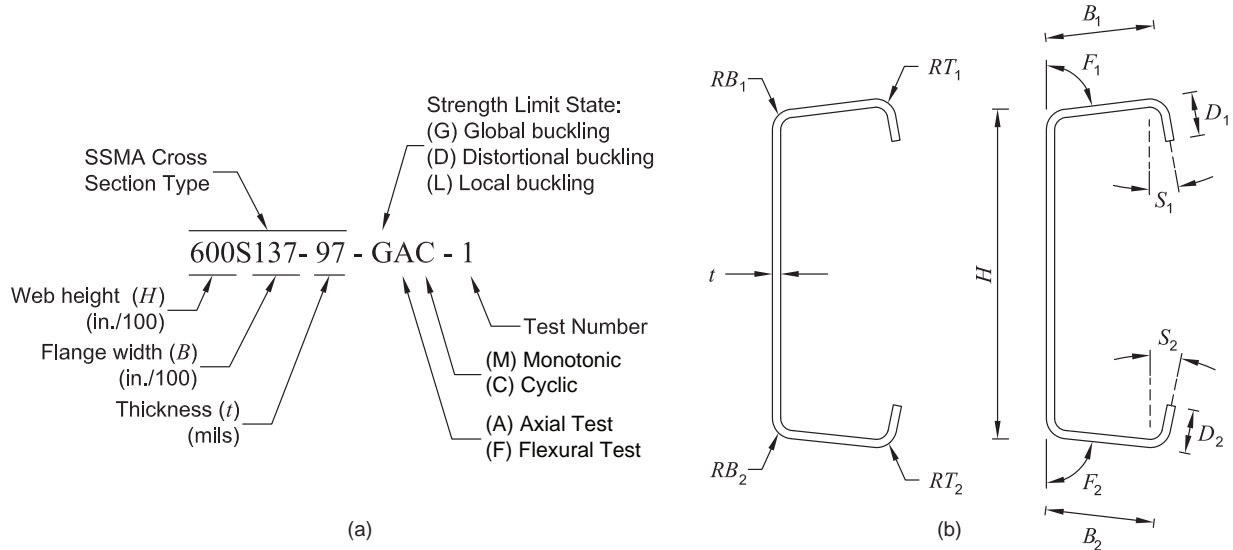


Figure 6: Specimen naming convention (a) and cross-section dimensions (b).

Imperfection magnitudes and shapes were computed following the procedures and imperfection reference system defined in Section 3. Photogrammetry measurements are also compared to the manual measurements.

#### 4.1. Maximum Imperfections

Maximum imperfection magnitudes were determined for all 20 members. Maximum imperfection magnitudes do not reflect the variation of imperfections along the length of the member and are provided here as reference measurements for comparison to commonly accepted limits, including those defined in ASTM C955-09 standard (ASTM 2009). The tolerance in ASTM C955 for out-of-straightness imperfections is  $L/960$ , for local web and flange imperfections is  $1.59\text{mm}$ ; and for twist  $L/384$  (max  $12.7\text{mm}$ ). Measurement statistics are summarized in Table 1 for each imperfection type, measurement method, and targeted buckling mode in the AISI project. The average maximum measured imperfections were generally smaller than these tolerances (see *mean* values in Table 1).

Table 1: Maximum imperfection magnitudes (photogrammetry and manual methods).

		Weak Axis Out-of- Straightness	Strong Axis Out-of- Straightness	Twist	Local Web	Local Flange (East)	Local Flange (West)	
		$\delta_B/L$ ( $\times 10^{-3}$ )	$\delta_C/L$ ( $\times 10^{-3}$ )	$\phi$ ( $^\circ$ )	$\delta_W/H$ ( $\times 10^{-3}$ )	$\delta_{FE}/B_E$ ( $\times 10^{-3}$ )	$\delta_{FW}/B_W$ ( $\times 10^{-3}$ )	
Manual	Global (n=4)	Mean	0.55 (L/1813)	-	0.99	2.79 (H/359)	25.88 (B/39)	40.36 (B/25)
		Max.	0.97 (L/1035)	-	1.76	5.24 (H/191)	40.52 (B/25)	51.57 (B/19)
		Min.	0.25 (L/3970)	-	0.25	1.59 (H/628)	0.65 (B/1527)	21.92 (B/46)
		St.Dev.	0.11	-	0.09	0.70	10.96	5.20
		COV	0.14	-	0.24	0.19	0.54	0.17
	Local (n=8)	Mean	0.37 (L/2740)	-	0.55	4.29 (H/233)	23.76 (B/42)	28.42 (B/35)
		Max.	0.68 (L/1465)	-	2.16	9.93 (H/101)	65.36 (B/15)	39.14 (B/26)
		Min.	0.24 (L/4226)	-	0.14	1.53 (H/653)	2.73 (B/367)	8.36 (B/120)
		St.Dev.	0.13	-	0.42	3.11	12.07	10.11
		COV	0.33	-	0.54	0.73	0.57	0.38
	Distortional (n=8)	Mean	0.46 (L/2193)	-	0.75	3.32 (H/301)	27.24 (B/37)	25.72 (B/39)
		Max.	0.97 (L/1028)	-	2.28	5.45 (H/183)	64.82 (B/15)	70.55 (B/14)
		Min.	0.22 (L/4513)	-	0.10	0.63 (H/1597)	8.59 (B/116)	5.35 (B/187)
		St.Dev.	0.16	-	0.48	1.35	9.46	13.81
		COV	0.33	-	0.57	0.43	0.29	0.47
Photogrammetry	Global (n=4)	Mean	0.92 (L/1090)	0.50 (L/1987)	1.06	3.95 (H/253)	39.42 (B/25)	68.38 (B/15)
		Max.	1.71 (L/586)	0.64 (L/1572)	1.69	5.89 (H/170)	55.48 (B/18)	80.53 (B/12)
		Min.	0.38 (L/2636)	0.24 (L/4246)	0.41	3.14 (H/319)	29.42 (B/34)	45.33 (B/22)
		St.Dev.	0.19	0.10	0.06	0.84	7.53	9.86
		COV	0.14	0.25	0.12	0.21	0.19	0.15
	Local (n=8)	Mean	0.76 (L/1312)	6.28 (L/159)	0.71	5.57 (H/179)	31.10 (B/32)	34.96 (B/29)
		Max.	1.94 (L/516)	18.33 (L/55)	2.06	11.81 (H/85)	63.67 (B/16)	49.69 (B/20)
		Min.	0.32 (L/3087)	0.39 (L/2548)	0.34	2.32 (H/432)	15.06 (B/66)	18.69 (B/54)
		St.Dev.	0.35	2.79	0.38	3.20	9.09	10.72
		COV	0.42	0.56	0.45	0.57	0.25	0.30
	Distortional (n=8)	Mean	0.62 (L/1613)	0.95 (L/1052)	0.75	3.83 (H/261)	28.98 (B/35)	33.41 (B/30)
		Max.	0.99 (L/1009)	1.34 (L/746)	1.66	6.61 (H/151)	60.08 (B/17)	73.25 (B/14)
		Min.	0.22 (L/4543)	0.26 (L/3880)	0.22	0.75 (H/1339)	15.09 (B/66)	14.12 (B/71)
		St.Dev.	0.12	0.38	0.34	1.50	11.21	11.41
		COV	0.24	0.41	0.41	0.41	0.35	0.29

$L$  = specimen length;  $H$  = web width;  $B_E$  = east flange width;  $B_W$  = west flange width;

$n$  = number of specimens in the group.

Maximum imperfections are compared to ASTM C955-09 tolerances in Fig. 7. Results show that most maximum imperfections fall below the ASTM C955-09 limits, and that out-of-straightness imperfections generally increase with length (Fig. 7a and Fig. 7b). Global imperfections magnitudes increase with sheet thickness because of the plastic strains caused by coiling of the sheet for transportation and manufacturing. Initial twist in longer members was less than the ASTM limits while for short members with narrow webs twist tended to have imperfections greater than the ASTM tolerance. Fig. 7d shows that local web imperfections typically increase with web slenderness ( $H/t$ ), and Fig. 7e shows that flange imperfections generally decrease with flange slenderness ( $B/t$ ). These trends are associated to through-thickness nonlinear residual stresses and elastic spring-back from the cold formed bending of the flanges (Moen et al. 2008).

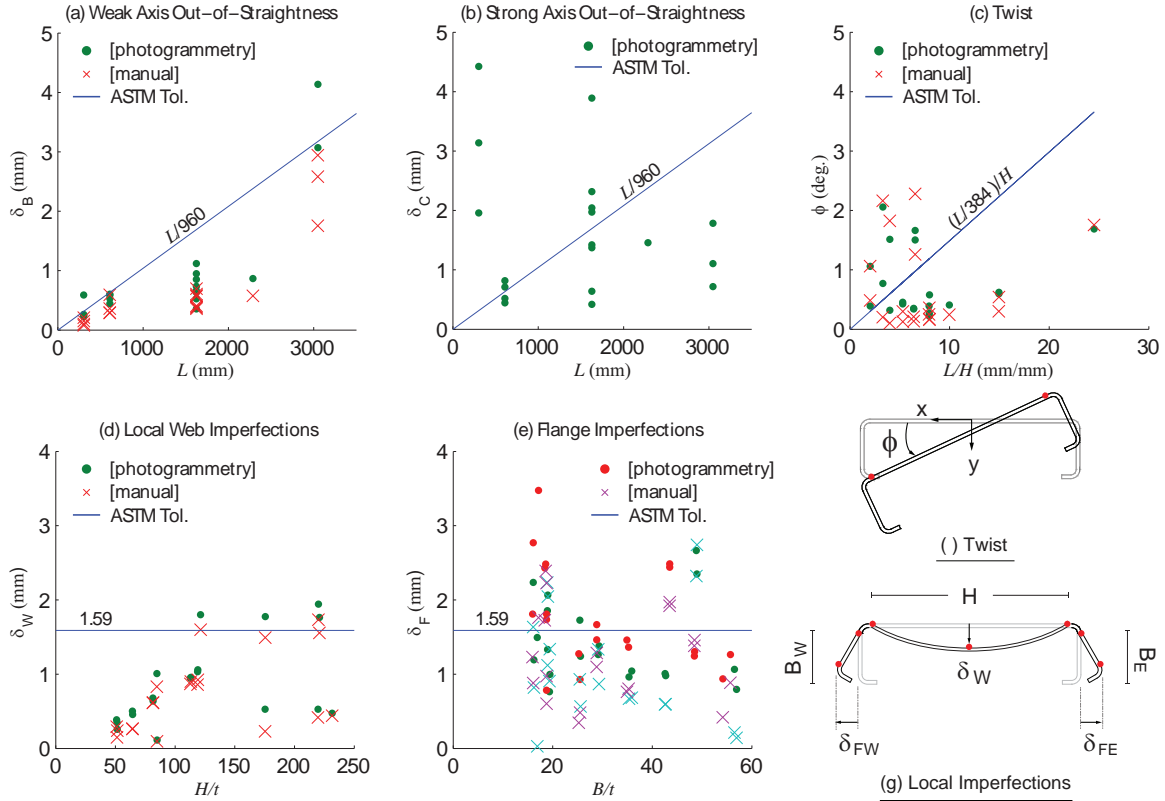


Figure 7: Maximum imperfections and ASTM C955-09 tolerance limits.

#### 4.2. Imperfection Shapes

Global and local imperfection shapes for specimen 362S137-68-DAM-2 ( $L=609.6\text{mm}$ ) are plotted in Fig. 8 and Fig. 9. Local imperfections shapes ( $\delta_W$ ,  $\delta_{FE}$ , and  $\delta_{FW}$ ) vary along the length because of residual stresses induced by the cold forming process and elastic spring-back (Moen et al. 2008). The spring-back is greater at the ends of the members due to the decreased cross-sectional restraint yielding greater cross-sectional imperfections, as shown in Fig. 9, and resulting in opening of the cross-section. Additional imperfections can be induced in the members during transportation and/or installation specially when connecting them to other members/pieces. The specimens in this study had 15.9mm end plates welded at both ends that could increase the cross-sectional imperfections magnitudes towards the ends due to the thermal expansion during welding, see Fig. 9. The imperfection shapes obtained using the photogrammetry and manual measurement methods for all 20 specimens are qualitatively consistent (see Fig. 8 and Fig. 9) and they are compared to explore the accuracy of the photogrammetry method in the next section.

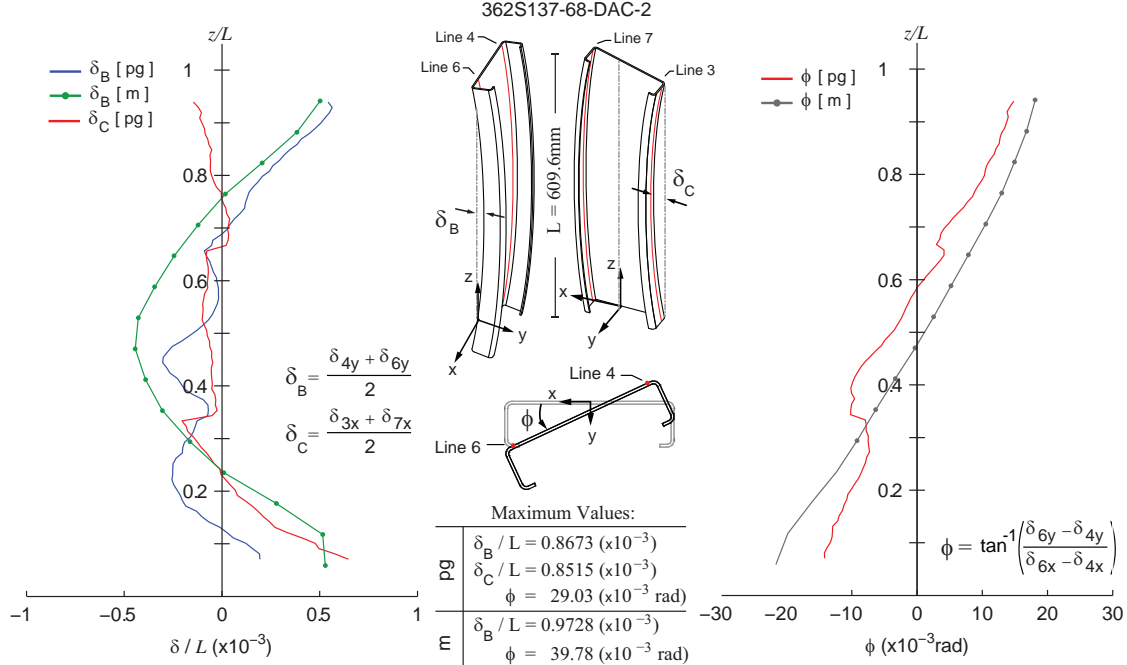


Figure 7: Global imperfections for specimen 362S137-68-DAM-2 (pg = photogrammetry, m = manual).

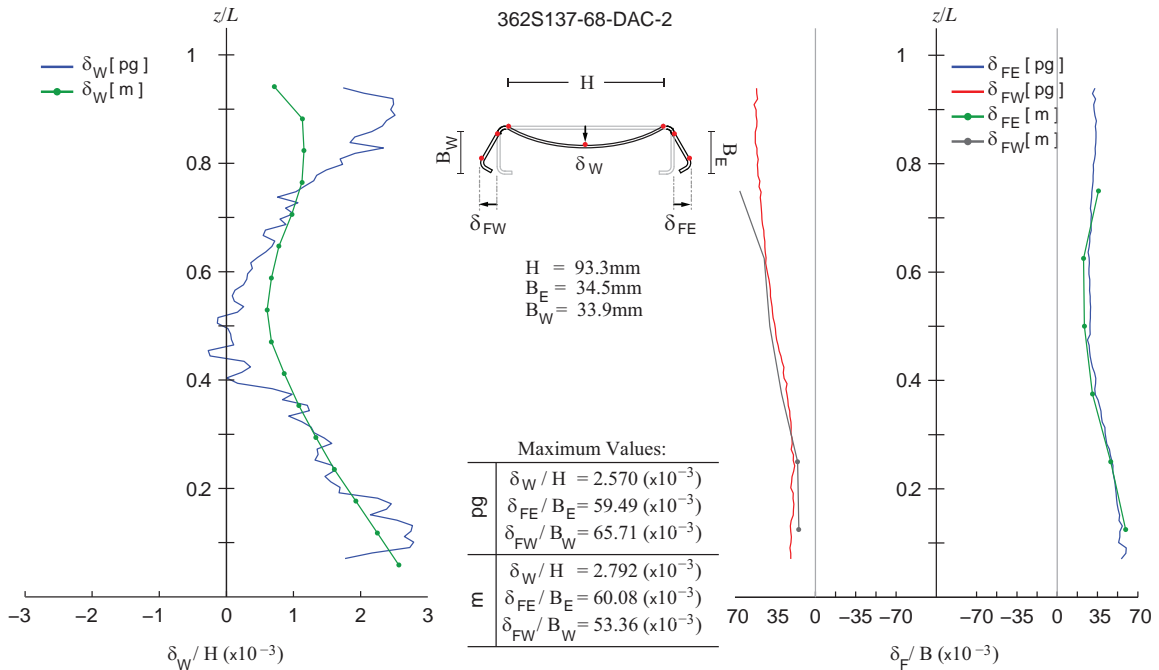


Figure 8: Local imperfections for Specimen 362S137-68-DAM-2 (pg = photogrammetry, m = manual).

### 4.3 Non-Contact Measurement Error Quantification

A common question when using non-contact measurement techniques such as photogrammetry and laser scanning is, ‘how accurate are they relative to traditional manual methods e.g., dial gauge measurements?’ References or standards to establish the measurement error when using non-contact methods do not exist and confidence intervals for these need to be defined. In this section, imperfection measurements obtained with the photogrammetry and manual measurement

methods are compared to explore the accuracy of the photogrammetry method. The following approach is presented here for photogrammetry, but it is written in a general format that is applicable to evaluate accuracy of any 3D non-contact measurement method, for example, the laser scanning method described in Section 2.2.

The accepted practice for measuring imperfections is the use of a manual measurement method, such as the one introduced in Section 2. The measurement error of this manual method  $e_m$ , can be calculated from the precision of the dial gages and out-of-straightness variability of the precision rail. Other sources of error such as the associated with variability and repeatability in measurements were not considered here. Measurement errors for the 3D non-contact method, e.g., for photogrammetry  $e_p$ , can be defined either by the manufacturer of the equipment or by the user. The underlying hypotheses for the error assumptions for the non-contact measurement method (i.e. photogrammetry) are validated if the difference/error in imperfection measurements between techniques for a specific specimen  $e_d$  is less than the *maximum expected error*,  $e_m+e_p$ . The differential error  $e_d$  for an imperfection quantity is calculated as the absolute value of the difference between corresponding photogrammetry and manual measurements

$$e_d = |p_i - m_i| \quad (1)$$

where  $p_i$  and  $m_i$  are respectively the photogrammetry measurement and manual measurement at a specific location along the member.

The *maximum expected error*  $e_m+e_p$  on the right side of Eq. (1), requires knowing the measurement errors of both photogrammetry and manual measurement method. The error for the photogrammetry measurements using PhotoModeler and the Nikon camera discussed in Section 2.1 was calculated in previous research as  $e_p=\pm 0.11\text{mm}$  over a 95% confidence interval with a carefully controlled measurement study on a flat granite slab (Orsa et al. 2011). The study considered different photogrammetry parameters including camera separation angle, number of overlapping points, and camera distance to photographed object. Two specific cases from Orsa's study were consistent with the approach used in this study. For these two cases the angle separation was  $45^\circ$ , more than 10 points overlap between pictures, camera distance of around 1220mm, and no field calibration. The average of the resulting accuracy values for the two cases was used as the maximum photogrammetry error at a single point (Orsa et al. 2011).

The measurement error for the manual measurements of out-of-straightness and twist as described in Section 2.3, is dependent on the dial gage reading accuracy and the running accuracy for the moving carriage on the high-precision rail. The dial gauge uncertainty with assumed 95% confidence interval is  $e_g=\pm 0.01\text{mm}$  as provided by the manufacturer. The high-precision rail running accuracy with a 95% confidence interval as provided by the manufacturer is  $e_r=\pm 0.03\text{mm/m}$ , where the error within each meter of length is assumed to be independent (Parker 2008).

Error propagation on the measurements is taken into account by determining the combined uncertainty for each imperfection measurement. For weak axis out-of-straightness ( $\delta_B$ ) and local web ( $\delta_w$ ) imperfections calculated using the manual method, the dial gauges and rail system combined measurement uncertainty  $e_{mw}$  for each measurement is (Jimenez-Mejía 2009),

$$e_{mw} = \sqrt{n(e_g^2 + e_r^2)} \quad (2)$$

where  $e_g$  and  $e_r$  are the dial gauge and high-precision rail uncertainties, respectively; and  $n = 2$  for out-of- straightness ( $\delta_B$ ) and  $n = 3$  for local web ( $\delta_w$ ) imperfections. Similarly, the combined measurement uncertainty  $e_{pw}$  when calculating the out-of-straightness and local web imperfection magnitudes using photogrammetry method is

$$e_{pw} = \sqrt{ne_p^2} \quad (3)$$

where  $e_p$  is the maximum photogrammetry error at single point, and  $n = 2$  for out-of- straightness ( $\delta_B$ ) and  $n = 3$  for local web ( $\delta_w$ ) imperfections. The *maximum expected error* for weak axis out of straightness and local web imperfection magnitudes is obtained by adding Eq. (2) and (3) and is the same for all specimens.

Twist imperfection magnitudes ( $\phi$ ) calculated using the manual method were affected by the dial gauges and rail system uncertainty and a high-precision ruler precision ( $\pm 0.40\text{mm}$ ). The twist is calculated as  $\phi = \tan^{-1}(d/h)$ , where  $d$  is the difference between dial gauge readings along the y-axis at lines 4 and 6, and  $h$  is the measured distance between dial gauges along the x-axis at lines 4 and 6, as illustrated in Fig. 3. Therefore, the dial gauges and rail system combined measurement uncertainty  $e_{m\phi}$  corresponding to twist imperfections from the manual method is (Jimenez-Mejía 2009)

$$e_{m\phi} = \sqrt{\left(\frac{\partial\phi}{\partial d}e_d\right)^2 + \left(\frac{\partial\phi}{\partial h}e_h\right)^2} \quad (4)$$

where  $\partial\phi/\partial d$  and  $\partial\phi/\partial h$  are the partial derivatives of the twist ( $\phi$ ) with respect to  $d$  and  $h$  respectively;  $e_d = e_{mw}$  (with  $n = 2$ ) from Eq. (2); and  $e_h$  is the  $h$  dimension uncertainty, which was manually measured with a precision ruler. The combined measurement uncertainty  $e_{p\phi}$  for the photogrammetry method corresponding to twist imperfections is obtained in a similar way as in the manual method where the uncertainty on the distance  $d$  in Eq. (4) is replaced by the uncertainty value given by Eq. (3) [ $n=2$ ]

$$e_{p\phi} = \sqrt{\left(\frac{\partial\phi}{\partial d}\sqrt{2}e_p\right)^2 + \left(\frac{\partial\phi}{\partial h}e_p\right)^2} \quad (5)$$

Because  $d$  and  $h$  values vary for each specimen, the uncertainties for twist calculations vary between specimens as well. The *maximum expected error* for twist imperfection magnitudes is obtained by adding Eq. (4) and (5).

Flange imperfection magnitudes are calculated as  $\delta_F = B\cos(F)$  for the east and west flanges using the measured specimen dimensions in Table A1. A caliper ( $e_B = \pm 0.003\text{mm}$ ) was used to measure flange widths  $B_E$  and  $B_W$ , while a digital level ( $e_F = \pm 0.01$  degrees) was used to measure flange angles  $F_E$  and  $F_W$  (see Fig. 6b). The combined measurement uncertainty  $e_{mf}$  for flange imperfections magnitudes calculated using the manual method is

$$e_{mf} = \sqrt{\left(\frac{\partial \delta_F}{\partial B} e_B\right)^2 + \left(\frac{\partial \delta_F}{\partial F} e_F\right)^2} \quad (6)$$

where  $\partial \delta_F / \partial B$  and  $\partial \delta_F / \partial F$  are the derivative partial derivatives of  $\delta_F$  with respect to  $B$  and  $F$  respectively;  $e_B$  is the caliper uncertainty ; and  $e_F$  is the digital level uncertainty . The combined measurement uncertainty  $e_{pf}$  for the photogrammetry method corresponding to flange imperfections is numerically equal to Eq. (3), i.e.,

$$e_{pf} = \sqrt{n e_p^2} \quad (7)$$

Flange uncertainty values differ for each specimen due to varying dimensions  $B$  and  $F$ . The *maximum expected error* for flange imperfections is obtained by adding Eq. (6) and (7).

Histograms of the *differential error to maximum expected error* ratio,  $e_d / (e_m + e_p)$  for each imperfection type are shown in Fig. 10. The resulting error distributions show that most differential errors are less than the corresponding *maximum expected error* (i.e.,  $e_d / (e_m + e_p) < 1$ ), thus, the underlying hypotheses for the assumptions regarding  $e_m$  and  $e_p$  are validated. In other words, the photogrammetry method can be used to measure imperfections with a confidence interval of 77% that the error will be bounded within the photogrammetry accuracy uncertainty assumed ( $e_p = \pm 0.11\text{mm}$ ). The greater scatter of the *differential error* values corresponding to twist imperfections drives down this confidence interval (see Fig. 10b). If twist imperfection data is omitted, the confidence interval increases to 92% which corresponds to the assumed accuracy uncertainty for the photogrammetry method in the framework of this study.

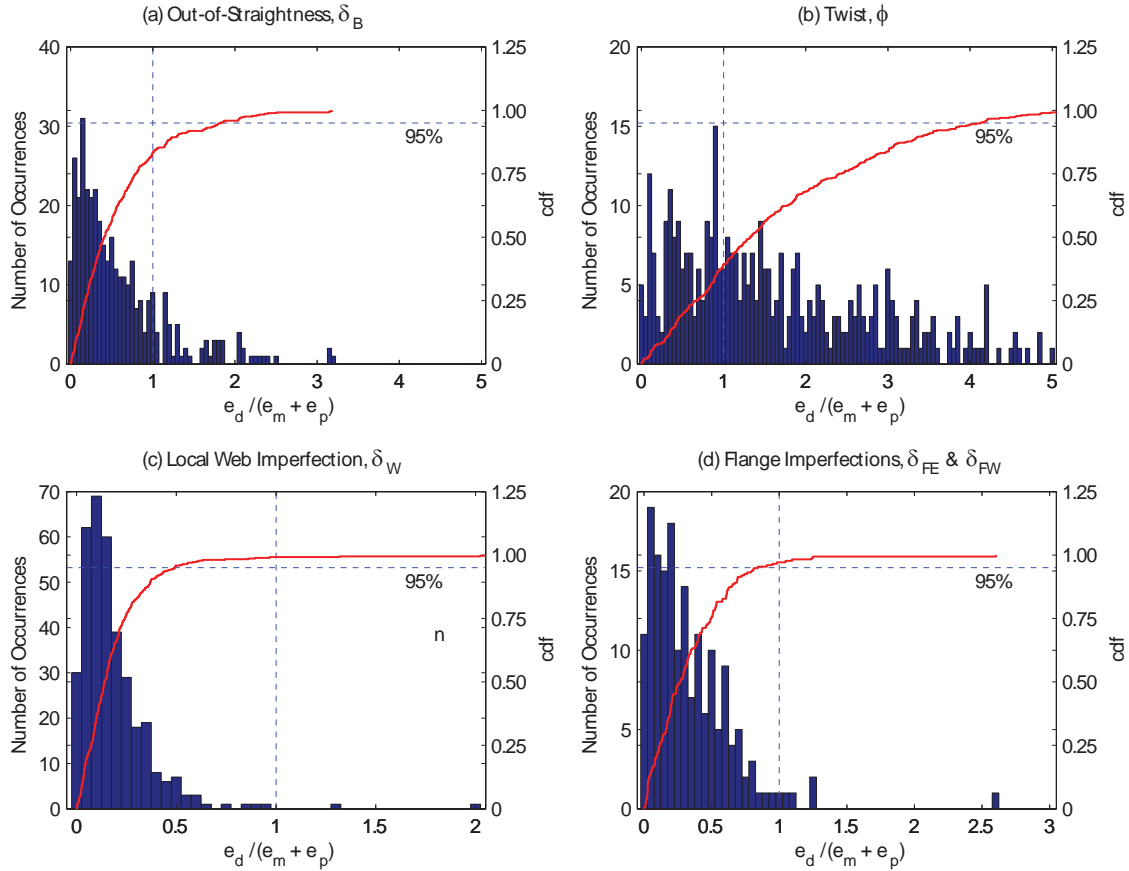


Figure 10: Histograms of the ratio of differential to *maximum expected error*.

## 5. Imperfection Measurement Study using Laser Scanning

The laser scanning method described in Section 2.2 was used to measured imperfections for four CFS members with lengths  $L=609\text{mm}$  to  $1219\text{mm}$ . The cross-section dimensions, as shown in Fig. 5b, are directly derived from the laser scanning readings every 3-mm along the specimen and averages are summarized in the Appendix, Table A2. All dimensions but thickness are taken by the laser scanner. The specimen naming convention is shown in Fig. 11.

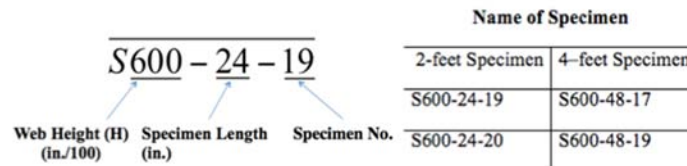


Figure 11: Specimen naming convention.

### 5.1. Maximum Imperfections

Global and local imperfections were estimated using the imperfection reference system and notation described in Section 3. For local imperfections however, the *perfect C-shaped cross-section* was determined by averaging the measured surface height  $y$  for the web and  $x$  of for the flanges in the reconstructed 3D point cloud. Local web imperfections are then calculated as the

difference between these plane and the height of the surface points running along the mid-web line, akin line 5 in Fig. 5a, as shown in Fig. 12. Flange imperfections are calculated in an analogous way (Fig. 12). The maximum global and local imperfections are summarized in Table 2.

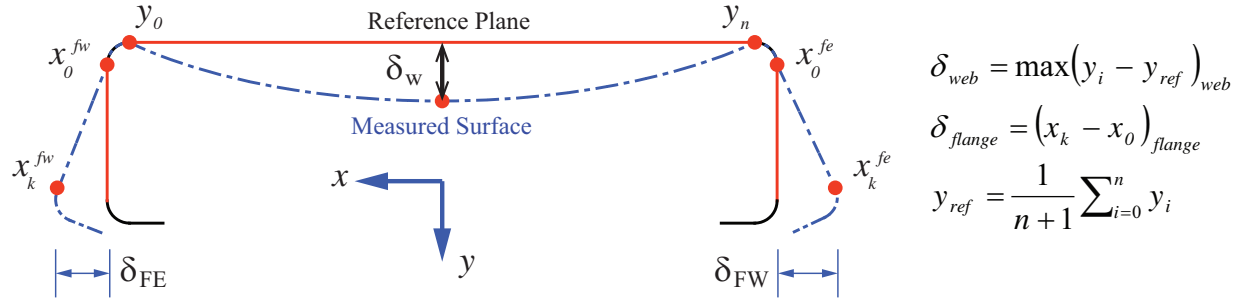


Figure 12: Local imperfection definition (laser scanning).

Table 2: Global and cross-sectional imperfections (laser scanning method).

Specimen	$\delta_B/L$ ( $\times 10^{-3}$ )	$\delta_C/L$ ( $\times 10^{-3}$ )	$\phi$ ( $^\circ$ )	$\delta_w/L$ ( $\times 10^{-3}$ )	$\delta_{FE}/L$ ( $\times 10^{-3}$ )	$\delta_{FW}/L$ ( $\times 10^{-3}$ )
S600-48-17	0.69 (L/1454)	3.13 (L/319)	0.34	0.39 (L/2566)	2.16 (L/463)	0.85 (L/1179)
S600-48-18	-0.78 (L/1274)	2.23 (L/448)	0.58	0.84 (L/1192)	-1.04 (L/957)	1.98 (L/505)
S600-24-19	-0.33 (L/3003)	2.70 (L/371)	-0.01	0.23 (L/4263)	0.68 (L/1461)	3.56 (L/281)
S600-24-20	0.56 (L/1789)	3.34 (L/299)	-0.40	0.27 (L/3717)	58.74 (L/17)	-0.30 (L/3283)

## 5.2. Imperfection Shapes

Large point clouds obtained using the laser scanning method allow precise calculation of member local and global imperfections shapes. Imperfections magnitudes profiles were collected every 3mm for the four specimens. An example of the calculated imperfection shapes is shown in Fig. 13 and Fig. 14 for specimen S600-48-18 ( $L=609.6\text{mm}$ ). First buckling mode curves (dashed line), were also fit to the global imperfection profiles.

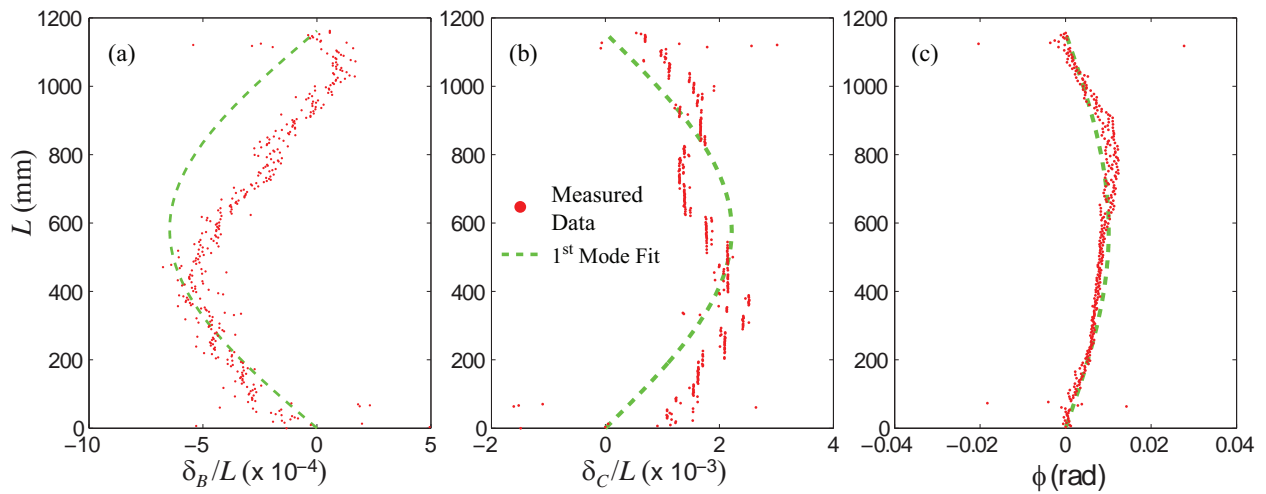


Figure 13: Out of straightness in weak axis (a), strong axis (b) and twist (c) for the S600-48-18 specimen.

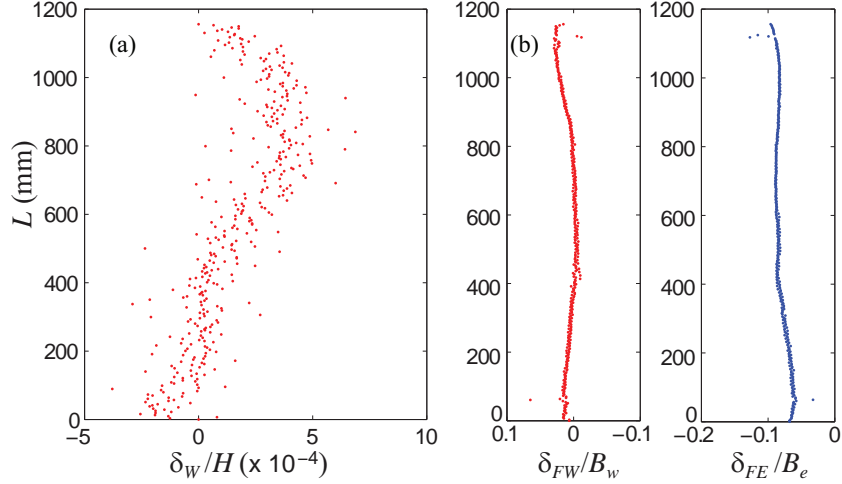


Figure 14: Local web (a) and flange (b) imperfections for the S600-48-18 specimen.

### 5.3 Laser Measurement Error Estimation

Sources of laser measurement errors are various. Laser scanners are always sensitive to the working environment. Ambient light could always impact accuracy of laser measurements, especially for the cold-formed steel members because of the reflectivity of their surface. It is recommended therefore to keep the room dim when taking measurements. Another source of error comes from how smooth the supporting frame and laser sensor ride along on the linear drive system. The setup was assembled such that the readings were not affected by these two issues. A third source of error comes from the laser sensor itself and can be quantified from its properties as provided by the manufacturer. The measurement error is proportional to the measured range, i.e., the width of the laser light beam projected on the measured surface and the distance from the sensor to such surface (Keyence 2012). The distance to the surface directly affects the repeatability factors and thus the accuracy. The imperfection measurements error for the four specimens measured is summarized in Table 3.

Table 3: Measurement error estimation.

Specimen	Web	Flange	Lips
Width (mm)	152.4	41.275	12.7
Linearity	0.05%	0.05%	0.05%
Error	0.0762	0.0206	0.0064

## 6. Imperfection Characterization Method

Imperfections measurements from the photogrammetry method were used to characterize specimen imperfect geometry as trigonometric series that describe imperfection magnitudes that are superposed to the geometry of a perfect cross-section. This type of characterization makes it possible to represent the initial geometry with a limited set of variables as opposed to use a large 3D point cloud. The initial geometry including imperfections can be reconstructed by modifying the geometry of the perfect cross-section in Fig. 11a such that the coordinates of points 2 to 8 match the shapes of the imperfections  $\delta_B$ ,  $\delta_C$ ,  $\phi$ ,  $\delta_w$ ,  $\delta_{FE}$ , and  $\delta_{FW}$ . For local web imperfections for example, the geometry is modified such that the out-of-plane deformation at any point along line

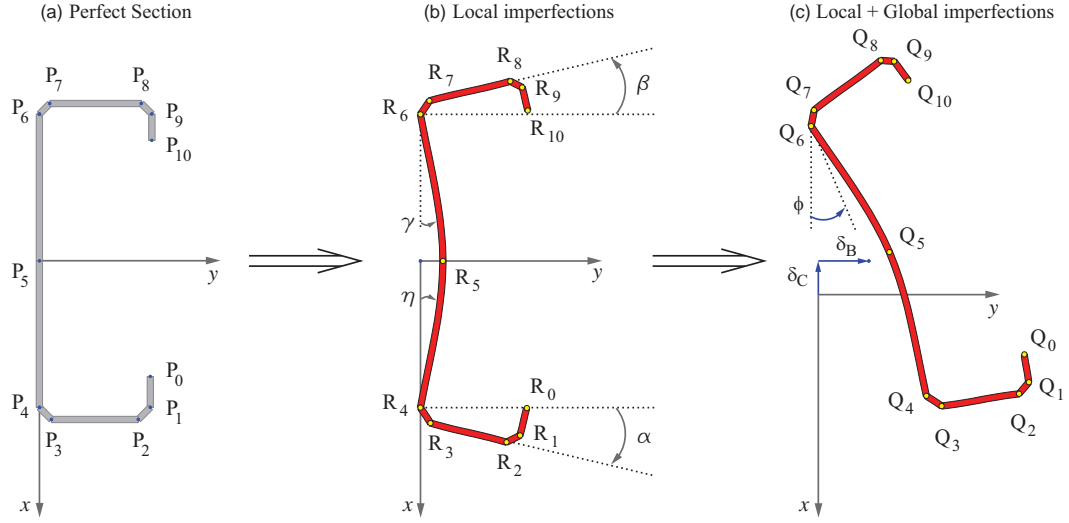
5 (i.e., P5 in Fig. 4.8a) is equal to  $\delta_w$ . The first step for this characterization requires a continuum representation of the imperfection magnitudes along the length. A sine-wave consisting of four terms plus a linear term was fit using a least-squares-approach to the measured imperfection shapes of the specimens listed in Table A2 as shown in Eq. 8

$$\delta_i(z) = (mz + b) + \sum_{k=1}^4 C_k \sin\left(\frac{\pi}{L_k} z + \varphi_k\right) \quad (9)$$

where  $mz+b$  is the linear fit of the member,  $C_k$ ,  $L_k$  and  $\varphi_k$  respectively are the amplitude, the half-wavelength, and the phase angle of each sine-wave term. The linear term ' $mz + b$ ' was subtracted from the data before fitting the sine-wave series in Eq. 8. The fitted parameters are provided in Tables A3 to A5 in the Appendix.

The procedure to impose initial imperfections on the perfect geometry of a member by modifying the geometry of a *perfect C-shaped cross-section* is depicted in Fig. 11. For each cross-section along the length of the member, the geometry of the imperfect geometry is derived by first applying the local deformations,  $\delta_w$ ,  $\delta_{FE}$ , and  $\delta_{FW}$ , to the *perfect C-shaped cross-section*, as depicted in Fig. 11b. The resulting geometry is then further modified by applying the global imperfections,  $\phi$ ,  $\delta_B$ ,  $\delta_C$ , as illustrated in Fig. 11c. The procedure demonstrated in Fig. 11 is repeated to impose imperfections for any cross-section along the member.

The procedure to impose imperfections described above allows to consistently apply imperfections on a perfect member by directly modifying the geometry of the cross section to match the imperfections magnitude profiles  $\delta(z)$ . This differs from the traditional modal and modal spectral approaches, where imperfections are imposed as a linear combination of buckling modes (e.g., Zeinoddini and Schafer 2012). Buckling mode calculations are not needed in the proposed procedure (Fig. 11) to impose imperfections, only systematic geometry transformations. Imperfection profiles  $\delta(z)$  can be of the form described by Eq. (8) or any other that can properly represent the corresponding imperfection magnitude profile. The geometric transformations depend on the cross-sections and the imperfection definitions; however, they only need to be set up once for a cross-section type, as it is shown in Fig. 11 for a channel section.



**Step 1:** Use Eq. (1) and Table 6 to obtain values of  $\delta_B, \delta_C, \phi, \delta_w, \delta_{fe}, \delta_{fw}$  for any cross section located at the  $z$ -coordinate along the member.

**Step 2:** Use values in Table 2 to obtain the perfect section geometry:

$$\begin{aligned}
 P_4 &= [(0.5H - RB_2) \ 0]^T & P_6 &= [-(0.5H - RB_1) \ 0]^T \\
 P_3 &= [0.5H \ RB_2]^T & P_7 &= [-0.5H \ RB_1]^T \\
 P_2 &= [0.5H \ (B_2 - RT_2)]^T & P_8 &= [-0.5H \ (B_2 - RT_1)]^T \\
 P_1 &= P_2 + [-RT_2 \ RT_2]^T & P_9 &= P_8 + [RT_1 \ RT_1]^T \\
 P_0 &= P_2 + [-D_2 \ RT_2]^T & P_{10} &= P_8 + [D_1 \ RT_1]^T \\
 P_5 &= [0 \ 0]^T
 \end{aligned}$$

**Step 3:** Apply local imperfections  $\delta_w, \delta_{fe}, \delta_{fw}$  from step 1

$$\begin{aligned}
 R_i &= T_\alpha (P_i - Z) + Z, \quad i = 0 \dots 3 \\
 R_j &= T_\beta (P_j + Z) - Z, \quad j = 7 \dots 10 \\
 R_4 &= P_4, \quad R_6 = P_6, \quad R_5 = [0 \ \delta_w]^T \\
 T_\alpha &= \begin{bmatrix} \cos \alpha & -\sin \alpha \\ \sin \alpha & \cos \alpha \end{bmatrix}, \quad T_\beta = \begin{bmatrix} \cos \beta & -\sin \beta \\ \sin \beta & \cos \beta \end{bmatrix} \\
 Z &= [0.5H \ 0]^T \\
 \alpha &= -\sin^{-1}(\delta_{fw}/(B_2 - RT_2)), \quad \beta = \sin^{-1}(\delta_{fe}/(B_1 - RT_1)) \\
 \gamma &= \tan^{-1}(3\delta_w/(H - 2RB_1)), \quad \eta = -\tan^{-1}(3\delta_w/(H - 2RB_2))
 \end{aligned}$$

**Step 4:** Apply global imperfections  $\delta_B, \delta_C, \phi$  from step 1

$$\begin{aligned}
 Q_k &= T_\phi R_k + [\delta_C \ \delta_B]^T, \quad k = 0 \dots 10 \\
 T_\phi &= \begin{bmatrix} \cos \phi & -\sin \phi \\ \sin \phi & \cos \phi \end{bmatrix}
 \end{aligned}$$

Figure 11: Imperfection reconstruction procedure.

## 7. Imperfections Database

The 3D imperfection field framework described in the previous sections is supported by an imperfections database hosted by the Cold-Formed Steel Research Consortium at [www.cfsrc.org](http://www.cfsrc.org). The database holds imperfection measurements of individual members in the form of  $x$ - $y$ - $z$  point clouds with a common origin at one end of the member and centered following the procedure outlined in Section 3. With each database entry, the researcher's name, supporting university, advising professor, publication date, and necessary contact information will be provided. The nominal dimensions and relevant specimen information will also be presented with each entry. Finally, the database will indicate the measurement method used, specify supporting publication references, and supply any additional information or attachments related to the point cloud. Each point cloud is stored as a single text file, and an Excel workbook explains the functionality of the database and summarizes the measurements included. Fig. A1 and A2 in the Appendix depict the interface of this database.

## 8. Conclusions

Initial geometric imperfections in cold-formed steel structural members can greatly affect their axial and flexural capacities. The ability to accurately measure, quantify, and model these

imperfections is essential to accurately predicting the strength of cold-formed steel members. This study proposed new methods for defining local, distortional, and global imperfections, and used three different measurement methods to quantify imperfection magnitudes in 24 different specimens. Imperfections were measured at many different cross-sections along a member's length, creating a full-field representation of each imperfect member. This study verifies the use of noncontact measurement methods, which provide many advantages, including a more detailed imperfection analysis of a member. A characterization method was also proposed, which allows for an imperfect member to be accurately represented with a series of sine terms rather than a large 3D point cloud, simplifying computational analysis. Finally, this research has significantly increased the amount of available imperfection data in cold-formed steel. In order to make this data more readily available, a communal database format has been proposed and will be implemented in the near future.

### Acknowledgements

The first two authors would like to extend their gratitude to the American Iron and Steel Institute (AISI) for supporting this project, and to ClarkDietrich Building Systems for donating the CFS specimens. The third author would like to extend thanks to National Science Foundation (NSF-CMMI-1235196) for founding her research. The views expressed in this work are those of the authors and not of NSF or AISI.

### References

- ASTM International (2009). "ASTM-C955, Standard Specification for Load-Bearing (Transverse and Axial) Steel Studs, Runners (Tracks), and Bracing or Bridging for Screw Application of Gypsum Panel Products and Metal Plaster Bases." West Conshohocken, PA.
- Godoy, L.A. (1996). "Thin-Walled Structures with Structural Imperfections: Analysis and Behavior". Pergamon Press, Oxford.
- Jimenez-Mejía, J.F. (2009). "Tratamiento de Datos Experimentales." National University of Colombia, Medellín, Colombia.
- Jolliffe, I. (2002). "Principal Component Analysis and Factor Analysis." (2002). *Principal Component Analysis*, Springer Series in Statistics, Springer New York, 150–166.
- Keyence. (2012). "LJ-V7000 High-speed 2D/3D laser scanner specification". Elmwood Park, NJ, USA.
- Koiter, W. T. (1945). "On the stability of elastic equilibrium", Ph.D. Thesis. Delft: NASA TT F.
- Liu, Y.-S., and Ramani, K. (2009). "Robust principal axes determination for point-based shapes using least median of squares." *Computer-Aided Design*, 41(4), 293–305.
- Moen, C.D., Igusa, T., Schafer, B.W. (2008). "Prediction of residual stresses and strains in cold-formed steel members." *Thin-Walled Structures*, 46 (11), 1274-1289.
- Orsa, R.J., Eatherton, M.R., Moen, C.D. (2011). "Using Close-Range Photogrammetry to Characterize Initial Imperfections of Cold Formed Steel Members." Research Report, Virginia Polytechnic Institute and State University, Blacksburg, VA.
- Padilla-Llano, D.A., Moen, C.D., Eatherton, M.R. (2013). "Energy Dissipation of Thin-Walled Cold-Formed Steel Members." Research Report, Virginia Polytechnic Institute and State University, Blacksburg, VA.
- Parker ORIGA Corporation (2008). "Aluminum Roller Guides." ORIGA Corporation, Glendale Heights, IL.
- Peterman, K.D. (2012). "Experiments on the Stability of Sheathed Cold-Formed Steel Studs Under Axial Load and Bending." Master's Thesis, Johns Hopkins University, Baltimore, MD.
- Eos Systems Inc. (2012). *PhotoModeler*. Build: 2012.1.1.668.
- Quach, W.M., Teng, J.G., Chung, K.F. (2004). "Residual stresses in steel sheets due to coiling and uncoiling: a closed-form analytical solution." *Engineering Structures*, 26, 1249-1259.
- Rasmussen, K. J. R., and Hancock, G. J. (1988). "Geometric imperfections in plated structures subject to interaction between buckling modes." *Thin-Walled Structures*, 6(6), 433–452.

- Schafer, B.W., Li, Z., Moen, C.D. (2010). "Computational modeling of cold-formed steel." *Thin-Walled Structures*, 48 (10-11), 752-762.
- Schafer, B.W., Peköz, T. (1998). "Computational modeling of cold-formed steel: characterizing geometric imperfections and residual stresses." *Journal of Constructional Steel Research*, Vol. 47, 193-210.
- Young, B., Rasmussen, K.J.R. (1999). "Behaviour of cold-formed singly symmetric columns." *Thin-Walled Structures*. 33 (2) 83-102.
- Zeinoddini, V.M. (2011). "Geometric Imperfections in Cold-Formed Steel Members." Ph.D. Dissertation, Johns Hopkins University, Baltimore, MD.
- Zeinoddini, V.M. (2012). "Simulation of geometric imperfections in cold-formed steel members using spectral representation approach." *Thin-Walled Structures*, 60, 105-117.

## Appendix

Table A1: Measured specimen dimensions (photogrammetry and manual methods).

Specimen	$L$ (mm)	$D_E$ (mm)	$D_W$ (mm)	$B_E$ (mm)	$B_W$ (mm)	$H$ (mm)	$RT_E$ (mm)	$RT_W$ (mm)	$RB_E$ (mm)	$RB_W$ (mm)	$F_E$ (°)	$F_W$ (°)	$S_E$ (°)	$S_W$ (°)	$t$ (mm)
362S137-68-GAC-2	2286	11.8	13.3	34.4	33.4	93.3	4.0	4.0	4.4	4.4	88.5	88.2	-2.5	4.1	1.82
800S162-97-GFC-2	3048	12.0	13.4	40.4	40.3	203.9	4.8	5.2	5.4	5.2	90.1	88.6	0.3	2.2	2.50
800S162-97-GFM-2	3048	12.2	13.6	40.2	40.0	203.8	4.8	5.2	5.4	5.2	88.6	87.8	0.1	2.0	2.51
1200S162-97-GFC-1	3048	9.8	11.2	42.7	43.2	305.6	4.8	5.2	5.5	5.5	91.4	87.7	-3.4	0.4	2.52
362S162-54-LAM-2	305	11.7	12.2	42.3	41.6	92.7	4.2	4.4	3.6	4.4	89.2	89.2	3.2	2.2	1.44
362S162-54-LAC-1	305	11.7	11.8	42.0	41.6	92.7	4.0	4.4	3.6	4.4	88.9	89.5	1.0	2.0	1.44
600S162-33-LAM-2	305	13.0	13.5	42.0	41.5	150.3	3.6	4.0	3.6	4.4	88.1	91.9	2.0	-0.2	0.86
600S162-33-LAC-2	305	12.7	13.6	41.9	41.5	150.3	3.6	4.0	3.2	4.4	86.6	89.1	3.1	3.6	0.86
800S200-33-LFM-2	1626	14.6	14.7	50.1	49.8	204.6	3.6	3.6	3.1	3.2	91.3	89.4	-0.6	0.8	0.88
800S200-33-LFC-2	1626	13.9	14.3	52.8	50.3	203.7	3.6	4.4	3.2	3.2	89.7	90.7	-0.8	0.9	0.95
1000S200-43-LFC-2	1626	10.3	12.0	49.1	50.0	254.4	3.6	3.6	3.2	3.6	90.4	87.0	0.5	1.5	1.15
1000S200-43-LFM-2	1626	10.2	12.0	49.2	50.3	254.5	3.6	3.6	3.2	3.6	90.3	87.2	0.8	1.6	1.16
362S137-68-DAM-2	610	12.0	12.9	34.5	33.9	93.3	4.0	4.0	4.4	4.4	89.8	86.4	-2.0	4.2	1.82
362S137-68-DAC-2	610	11.6	13.4	34.4	33.9	93.2	4.0	4.0	4.4	4.4	89.7	86.2	-2.1	4.0	1.81
600S137-68-DAM-2	610	10.7	11.5	34.8	33.8	152.7	4.0	4.0	4.4	4.0	90.5	89.5	-1.4	-0.7	1.80
600S137-68-DAC-2	610	10.5	11.9	34.9	33.8	152.5	4.0	4.0	4.4	4.2	89.9	89.6	-1.1	-0.1	1.80
800S250-68-DFC-2	1626	14.5	11.9	64.3	63.2	204.1	8.7	4.1	6.1	4.0	90.6	90.6	-4.1	-3.9	1.80
800S250-68-DFM-2	1626	14.4	12.1	64.4	63.6	204.2	4.4	4.0	4.4	4.0	90.8	90.6	-4.8	-4.2	1.84
1200S250-97-DFC-1	1626	12.8	14.4	65.7	65.7	306.5	5.2	5.6	5.6	5.6	92.1	89.7	-4.6	-3.6	2.57
1200S250-97-DFM-1	1626	12.7	14.6	65.1	65.9	306.7	5.2	5.6	5.6	5.6	92.5	89.6	-5.1	-2.7	2.58

Table A2: Dimensions from laser scanner measurements.

Specimen	S600-48-17	S600-48-18	S600-24-19	S600-24-20
<b>H (mm)</b>	151.613	150.522	147.428	148.024
<b>Bw (mm)</b>	37.798	37.126	38.195	38.169
<b>Be (mm)</b>	41.148	39.127	37.855	40.107
<b>Dw (mm)</b>	10.262	11.918	10.955	9.813
<b>De (mm)</b>	10.702	10.924	8.591	9.416
<b>Fw (deg)</b>	82.505	86.42	-85.863	-32.284
<b>Fe (deg)</b>	-84.224	86.983	44.132	85.271
<b>Sw (mm)</b>	5.467	12.12	13.205	18.562
<b>Se (mm)</b>	13.415	17.526	19.358	10.285
<b>Rw (mm)</b>	4.361	3.728	3.645	3.709
<b>Rbe (mm)</b>	3.282	3.223	5.387	5.857
<b>Rtw (mm)</b>	3.884	5.098	7.244	3.729
<b>Rte (mm)</b>	3.446	8.835	6.601	8.076
<b>Data amount</b>	365	364	176	176

Note: Data amount indicates how many measurement values used to estimate average of dimensions for the specimen

Table A3: Imperfection fitted coefficients - global specimens.

	$L_1$	$L_2$	$L_3$	$L_4$	$C_1$	$C_2$	$C_3$	$C_4$	$\varphi_1$	$\varphi_2$	$\varphi_3$	$\varphi_4$	$m$	$b$	$R^2$	$adjR^2$	$SSE$	$RMSE$	
	(mm)				(mm) or ( $^\circ$ )				(rad)				(mm/mm) or ( $^\circ$ /mm)	(mm) or ( $^\circ$ )					
362SI37-68-GA-C-2	$\delta_B$	988.1	540.6	179.9	348.7	0.210	0.174	0.032	0.009	0.571	3.142	3.091	-0.435	1.36E-04	-0.170	0.995	0.995	3.92E-02	1.64E-02
	$\delta_C$	757.7	533.5	419.6	252.8	0.349	0.254	0.143	0.034	-0.547	0.527	1.482	-0.013	-7.53E-04	0.940	0.997	0.996	1.30E-02	9.50E-03
	$\phi$	863.5	484.6	300.9	140.9	0.619	0.293	0.114	0.023	0.066	-0.252	-0.743	1.862	1.82E-04	-0.264	0.999	0.999	1.86E-02	1.13E-02
	$\delta_w$	837.0	314.3	413.5	261.9	0.060	0.060	0.048	0.029	-3.140	1.981	1.621	3.131	-6.19E-05	-0.002	0.979	0.978	1.07E-02	8.60E-03
	$\delta_{FE}$	916.1	435.8	245.7	38.0	0.225	0.118	0.087	0.003	0.557	-3.142	-0.432	3.142	2.90E-04	-1.188	0.995	0.995	2.69E-02	1.36E-02
$\delta_{FW}$	686.1	315.6	480.5	254.6	0.078	0.078	0.042	0.041	1.556	1.992	-3.142	1.789	-3.85E-05	1.447	0.961	0.959	2.57E-02	1.32E-02	
800SI62-97-GFC-2	$\delta_B$	1410.3	844.2	577.9	461.6	1.729	0.681	0.254	0.085	1.358	1.941	2.350	3.141	4.70E-06	-0.007	0.999	0.999	8.45E-01	4.19E-02
	$\delta_C$	1542.0	466.7	532.6	338.9	0.311	0.152	0.106	0.040	-1.537	-1.475	-3.142	-0.281	3.78E-04	-0.579	0.997	0.997	7.96E-02	1.29E-02
	$\phi$	1347.4	608.8	336.7	545.1	0.085	0.059	0.015	0.001	1.112	-2.831	2.519	3.142	-1.52E-04	0.292	0.996	0.996	8.20E-03	4.10E-03
	$\delta_w$	1448.0	687.5	513.3	418.3	0.056	0.056	0.056	0.039	-1.569	-2.472	-1.714	-0.856	2.42E-05	0.508	0.976	0.976	4.49E-02	9.60E-03
	$\delta_{FE}$	490.7	406.5	599.0	1631.6	0.111	0.093	0.086	0.039	2.059	3.142	0.942	0.750	5.66E-05	-0.906	0.958	0.957	7.76E-02	1.27E-02
$\delta_{FW}$	628.3	1843.9	443.2	312.2	0.071	0.057	0.049	0.044	-3.142	-1.010	1.527	1.633	-3.87E-05	0.939	0.951	0.950	1.89E-01	1.98E-02	
800SI62-97-GFM-2	$\delta_B$	1336.4	838.5	584.6	406.5	1.508	0.694	0.159	0.065	1.266	2.414	3.142	2.757	-1.28E-04	0.188	1.000	1.000	1.16E-01	1.55E-02
	$\delta_C$	508.0	687.7	930.9	417.7	0.099	0.099	0.097	0.039	-1.247	-1.290	-2.222	-0.365	-1.54E-04	0.225	0.955	0.954	1.29E-01	1.63E-02
	$\phi$	1499.4	588.9	390.3	341.0	0.102	0.040	0.028	0.020	1.679	0.944	-3.142	-0.816	1.05E-04	0.016	0.984	0.984	5.25E-02	1.04E-02
	$\delta_w$	1435.4	499.5	664.4	392.3	0.058	0.058	0.057	0.018	-1.528	-1.459	-2.186	-0.811	1.98E-05	0.517	0.972	0.972	6.46E-02	1.15E-02
	$\delta_{FE}$	440.6	498.6	266.2	685.5	0.116	0.063	0.032	0.022	2.462	-0.198	1.916	-3.142	-3.23E-05	-1.585	0.895	0.893	3.47E-01	2.67E-02
$\delta_{FW}$	1352.7	541.8	859.8	303.7	0.177	0.108	0.068	0.020	-1.947	0.796	-0.963	-0.326	-5.91E-05	1.304	0.994	0.994	5.50E-02	1.07E-02	
1200SI62-97-GFC-1	$\delta_B$	1107.1	815.6	576.6	336.2	2.987	1.699	0.298	0.096	0.646	2.326	3.142	-0.116	-2.87E-04	0.412	0.999	0.999	4.92E-01	3.46E-02
	$\delta_C$	622.8	1275.1	451.2	272.2	0.194	0.156	0.116	0.044	-2.824	-1.949	-1.431	0.187	-6.73E-05	0.097	0.990	0.990	1.58E-01	1.97E-02
	$\phi$	498.8	1072.1	303.2	259.3	0.045	0.030	0.021	0.017	-3.142	0.219	-3.023	3.142	-8.86E-05	0.106	0.962	0.961	2.46E-02	7.70E-03
	$\delta_w$	1192.9	613.2	487.6	337.1	0.090	0.090	0.057	0.020	-1.978	-2.938	-1.569	3.142	7.71E-05	1.387	0.980	0.980	5.09E-02	1.11E-02
	$\delta_{FE}$	509.7	495.4	333.6	254.8	0.274	0.210	0.110	0.071	0.058	-3.142	-0.166	0.146	1.80E-04	-0.241	0.977	0.976	1.16E-01	1.68E-02
$\delta_{FW}$	326.0	711.2	231.3	1797.2	0.096	0.095	0.054	0.025	3.069	2.061	2.586	0.139	-7.44E-05	1.862	0.968	0.967	1.42E-01	1.86E-02	

Table A4: Imperfection fitted coefficients - local specimens.

	$L_1$	$L_2$	$L_3$	$L_4$	$C_1$	$C_2$	$C_3$	$C_4$	$\phi_1$	$\phi_2$	$\phi_3$	$\phi_4$	$m$	$b$	$R^2$	$adjR^2$	$SSE$	$RMSE$	
	(mm)				(mm) or ( $^\circ$ )				(rad)				(mm/mm) or ( $^\circ$ /mm)	(mm) or ( $^\circ$ )					
362SI62-54-LAM-2	$\delta_B$	120.1	221.5	36.8	23.7	0.078	0.019	0.014	0.004	0.882	-0.475	-2.122	3.141	2.51E-04	-0.038	0.998	0.997	2.02E-04	2.90E-03
	$\delta_C$	112.6	184.9	49.6	34.0	0.070	0.047	0.020	0.009	1.897	0.213	1.121	1.344	1.47E-02	-2.232	0.964	0.947	1.20E-03	7.10E-03
	$\phi$	86.2	304.8	42.7	30.1	0.126	0.036	0.027	0.009	1.840	1.319	3.142	3.142	-2.70E-03	0.482	0.997	0.996	9.41E-04	6.00E-03
	$\delta_w$	87.2	39.5	33.2	24.8	0.035	0.026	0.011	0.008	-0.371	-1.566	-1.278	3.141	3.70E-03	-0.454	0.993	0.989	2.08E-04	2.90E-03
	$\delta_{FE}$	112.6	119.9	51.6	42.4	0.104	0.054	0.031	0.019	-3.027	-2.146	1.868	3.142	-7.00E-03	0.783	0.999	0.998	6.04E-04	5.00E-03
$\delta_{FW}$	95.2	67.0	51.7	37.7	0.334	0.231	0.072	0.010	-0.286	0.938	2.289	3.061	8.90E-03	-1.009	1.000	1.000	1.79E-04	2.70E-03	
362SI62-54-LAC-1	$\delta_B$	71.3	86.3	59.9	6.9	0.143	0.114	0.059	0.001	0.468	-0.911	1.959	-2.271	-2.21E-04	0.033	0.993	0.990	5.78E-04	4.80E-03
	$\delta_C$	106.6	40.8	57.8	31.4	0.034	0.032	0.029	0.015	-2.596	1.910	-3.142	0.523	-2.55E-02	3.774	0.974	0.962	1.40E-03	7.40E-03
	$\phi$	49.1	38.8	127.5	32.6	0.041	0.025	0.025	0.007	-2.299	-1.877	1.545	0.126	9.10E-03	-1.202	0.984	0.977	6.23E-04	5.00E-03
	$\delta_w$	63.3	104.2	50.1	23.5	0.028	0.026	0.012	0.004	3.142	-2.946	3.142	0.144	2.30E-03	-0.105	0.971	0.960	5.36E-04	4.50E-03
	$\delta_{FE}$	46.3	54.2	101.8	41.1	0.175	0.161	0.110	0.065	1.023	-0.769	0.254	3.010	-6.00E-03	0.148	0.994	0.991	1.30E-03	7.10E-03
$\delta_{FW}$	114.7	55.2	28.3	20.3	0.096	0.021	0.019	0.014	-2.501	2.639	0.679	1.922	1.02E-02	-1.008	0.978	0.970	4.80E-03	1.36E-02	
600SI62-33-LAM-2	$\delta_B$	110.7	200.9	54.9	21.9	0.035	0.025	0.007	0.002	-0.733	-2.088	-0.663	-0.949	2.40E-03	-0.366	0.993	0.990	6.12E-05	1.60E-03
	$\delta_C$	66.4	73.9	304.7	31.1	0.041	0.035	0.030	0.006	2.962	-1.588	2.428	1.717	8.90E-03	-1.362	0.994	0.992	4.54E-04	4.40E-03
	$\phi$	98.5	41.9	174.0	38.6	0.093	0.063	0.046	0.037	-2.603	0.784	-2.199	2.873	3.80E-03	-0.431	0.995	0.992	1.10E-03	6.80E-03
	$\delta_w$	65.0	107.0	78.7	50.1	0.065	0.061	0.045	0.027	2.957	-3.142	-3.106	3.062	-4.00E-03	-0.633	0.987	0.982	1.80E-03	8.70E-03
	$\delta_{FE}$	40.7	50.1	111.8	32.2	0.081	0.077	0.066	0.024	2.508	1.267	-2.966	3.142	-7.00E-03	-0.316	0.977	0.968	3.80E-03	1.23E-02
$\delta_{FW}$	90.9	68.8	52.0	41.5	0.544	0.426	0.163	0.009	-0.637	1.089	2.089	3.142	-5.80E-03	0.151	1.000	1.000	3.54E-04	3.80E-03	
600SI62-33-LAC-2	$\delta_B$	92.9	64.0	46.1	39.0	0.066	0.063	0.028	0.013	-3.141	2.946	2.490	3.142	-9.56E-04	0.146	0.995	0.992	5.06E-04	4.50E-03
	$\delta_C$	104.7	62.6	50.2	36.1	0.073	0.064	0.047	0.011	-2.817	2.399	3.141	3.109	-2.08E-02	3.166	0.998	0.997	2.83E-04	3.30E-03
	$\phi$	111.6	56.8	44.5	35.4	0.054	0.030	0.026	0.015	-2.491	0.546	1.994	3.124	1.40E-03	-0.185	0.991	0.987	6.23E-04	5.00E-03
	$\delta_w$	39.6	112.7	46.6	34.3	0.099	0.093	0.072	0.045	1.212	-2.446	-0.368	2.633	3.00E-03	-0.513	0.997	0.996	5.35E-04	4.60E-03
	$\delta_{FE}$	117.0	54.4	66.1	40.6	0.208	0.171	0.154	0.062	-2.613	3.142	1.849	3.142	-8.20E-03	-0.246	0.998	0.998	1.80E-03	8.20E-03
$\delta_{FW}$	110.8	33.0	45.0	42.7	0.163	0.049	0.028	0.000	-2.744	-3.117	-0.056	-0.049	8.90E-03	-0.845	0.995	0.993	2.60E-03	1.03E-02	
800S200-33-LFM-2	$\delta_B$	916.5	358.3	1828.1	157.0	0.114	0.087	0.027	0.011	2.144	1.333	1.103	-0.692	-1.54E-05	0.012	0.998	0.998	7.10E-03	5.00E-03
	$\delta_C$	714.8	520.8	298.0	185.6	0.199	0.079	0.032	0.027	1.328	2.440	3.142	0.544	-7.05E-04	0.549	0.994	0.994	2.73E-02	9.70E-03
	$\phi$	411.2	221.3	286.8	1823.4	0.039	0.036	0.029	0.025	0.476	3.140	1.648	-0.975	-7.82E-05	-0.015	0.965	0.964	1.48E-02	7.20E-03
	$\delta_w$	468.2	564.3	251.0	174.0	0.163	0.123	0.108	0.032	0.051	-3.120	-2.863	-0.118	-3.08E-04	0.391	0.999	0.999	3.70E-03	3.60E-03
	$\delta_{FE}$	322.5	283.6	762.9	133.8	0.241	0.204	0.141	0.016	1.444	3.142	1.038	1.713	2.57E-04	0.013	0.993	0.993	4.04E-02	1.18E-02
$\delta_{FW}$	229.0	538.2	216.7	296.8	0.250	0.238	0.208	0.141	-2.149	-0.655	0.079	-3.142	-1.71E-04	1.017	0.982	0.981	1.96E-01	2.60E-02	
800S200-33-LFC-2	$\delta_B$	813.8	343.5	166.3	236.8	0.174	0.111	0.018	0.014	1.826	0.028	3.142	-1.361	-6.92E-05	0.054	0.999	0.999	7.70E-03	5.20E-03
	$\delta_C$	459.6	776.1	170.1	216.0	0.114	0.094	0.029	0.025	0.843	-2.154	1.503	1.940	2.06E-04	-0.161	0.995	0.995	2.01E-02	8.30E-03
	$\phi$	538.3	299.4	205.5	1828.8	0.086	0.068	0.031	0.009	-0.754	2.969	-1.564	2.627	-2.75E-04	-0.017	0.992	0.992	1.52E-02	7.30E-03
	$\delta_w$	795.1	223.4	292.4	152.4	0.287	0.019	0.018	0.013	-1.476	3.142	-2.958	1.923	-1.54E-04	0.275	0.998	0.998	2.49E-02	9.30E-03
	$\delta_{FE}$	702.6	408.6	286.6	230.1	0.271	0.271	0.073	0.038	1.287	1.812	2.274	3.142	1.63E-04	0.017	0.996	0.996	6.05E-02	1.45E-02
$\delta_{FW}$	764.4	409.4	278.8	150.8	0.442	0.119	0.044	0.039	-1.490	-2.096	3.142	-1.648	2.76E-04	0.205	0.988	0.988	4.30E-01	3.86E-02	
1000S200-43-LFC-2	$\delta_B$	846.8	240.4	482.2	210.0	0.281	0.100	0.070	0.061	-1.393	-3.142	3.142	-1.825	-2.92E-04	0.241	0.996	0.996	5.94E-02	1.46E-02
	$\delta_C$	536.2	306.8	1828.8	246.3	0.331	0.159	0.061	0.045	2.471	-0.364	-0.114	1.784	-2.10E-03	1.716	0.999	0.999	1.14E-02	6.40E-03
	$\phi$	363.0	284.8	801.0	183.0	0.058	0.057	0.050	0.021	2.253	3.142	-0.715	0.556	-4.83E-05	0.241	0.984	0.983	1.53E-02	7.40E-03
	$\delta_w$	808.2	253.9	231.7	329.8	0.353	0.353	0.241	0.208	-1.624	-2.389	-0.199	-3.142	8.09E-05	1.262	0.981	0.980	6.83E-01	4.92E-02
	$\delta_{FE}$	674.5	521.7	211.0	310.0	0.730	0.513	0.056	0.029	0.878	2.930	0.067	3.142	9.54E-05	-0.674	0.998	0.998	5.42E-02	1.39E-02
$\delta_{FW}$	787.1	366.7	341.3	213.8	0.381	0.381	0.341	0.060	-1.563	-3.113	-0.729	3.142	1.45E-04	1.799	0.982	0.982	5.53E-01	4.43E-02	
1000S200-43-LFM-2	$\delta_B$	330.1	345.9	754.8	181.7	0.275	0.144	0.122	0.018	1.683	-0.443	-1.892	2.083	3.32E-04	-0.275	0.984	0.984	1.07E-01	1.96E-02
	$\delta_C$	290.3	256.4	227.9	555.9	0.244	0.232	0.135	0.106	-1.770	0.261	2.275	-2.151	1.10E-03	-0.949	0.992	0.991	2.93E-02	1.03E-02
	$\phi$	302.8	318.6	206.2	1379.6	0.068	0.066	0.030	0.009	1.417	0.077	-2.816	3.142	3.39E-05	0.067	0.990	0.990	1.09E-02	6.30E-03
	$\delta_w$	251.4	809.6	229.9	326.7	0.329	0.329	0.225	0.220	-2.448	-1.640	-0.158	-3.142	-1.80E-04	1.596	0.984	0.983	5.10E-01	4.27E-02
	$\delta_{FE}$	712.7	563.5	360.1	135.7	0.668	0.331	0.073	0.011	1.040	3.142	1.100	0.819	2.52E-04	-0.801	0.999	0.999	1.78E-02	8.00E-03
$\delta_{FW}$	797.1	334.7	289.0	206.1	0.343	0.209	0.157	0.048	-1.601	-3.142	-1.320	3.142	-2.67E-04	2.187	0.982	0.981	4.98E-01	4.24E-02	

Table A5: Imperfection fitted coefficients - distortional specimens.

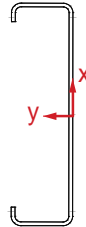
	$L_1$	$L_2$	$L_3$	$L_4$	$C_1$	$C_2$	$C_3$	$C_4$	$\varphi_1$	$\varphi_2$	$\varphi_3$	$\varphi_4$	$m$	$b$	$R^2$	$adjR^2$	$SSE$	$RMSE$	
	(mm)				(mm) or ( $^\circ$ )				(rad)				(mm/mm) or ( $^\circ$ /mm)	(mm) or ( $^\circ$ )					
362S137-68-DAM-2	$\delta_B$	224.2	178.2	99.9	63.7	0.366	0.282	0.021	0.013	0.421	2.570	2.450	3.142	2.29E-04	-0.070	1.000	1.000	7.53E-04	3.10E-03
	$\delta_C$	317.1	602.3	123.5	77.7	0.157	0.076	0.028	0.017	1.330	-0.987	0.585	1.029	-7.38E-04	0.225	0.995	0.994	3.70E-03	7.00E-03
	$\phi$	187.5	86.8	82.1	147.5	0.241	0.081	0.076	0.052	1.197	-2.716	-0.064	-1.847	3.30E-03	-0.881	0.998	0.998	5.70E-03	8.60E-03
	$\delta_w$	297.1	607.7	158.2	68.7	0.133	0.032	0.025	0.004	1.416	-0.156	1.762	-0.857	-4.32E-04	0.269	0.999	0.999	3.35E-04	2.10E-03
	$\delta_{FE}$	287.8	175.4	102.9	76.4	0.261	0.118	0.026	0.020	-1.725	3.142	3.142	3.142	1.50E-03	-1.534	0.998	0.997	1.11E-02	1.19E-02
$\delta_{FW}$	242.5	166.2	127.1	93.9	0.426	0.208	0.067	0.017	0.761	1.863	3.142	3.142	-1.70E-03	2.113	1.000	1.000	8.56E-04	3.30E-03	
362S137-68-DAC-2	$\delta_B$	234.9	146.3	103.7	75.3	0.157	0.113	0.048	0.028	0.635	1.224	1.555	0.077	6.07E-04	-0.187	0.997	0.997	2.50E-03	5.70E-03
	$\delta_C$	177.0	140.7	200.3	119.9	0.272	0.223	0.157	0.113	0.666	1.513	-1.058	2.879	-3.47E-04	0.107	0.996	0.996	1.70E-03	4.70E-03
	$\phi$	282.2	161.1	93.5	71.2	0.123	0.063	0.049	0.022	1.264	-0.516	2.502	-0.061	3.20E-03	-1.086	0.997	0.996	3.60E-03	6.90E-03
	$\delta_w$	292.7	609.0	90.5	141.7	0.132	0.027	0.014	0.010	1.431	0.333	0.722	1.648	-5.32E-05	0.130	0.998	0.998	9.18E-04	3.50E-03
	$\delta_{FE}$	267.1	94.7	93.7	56.5	0.277	0.201	0.189	0.004	-2.027	-1.549	1.368	-1.371	1.70E-03	-1.767	1.000	1.000	1.40E-03	4.30E-03
$\delta_{FW}$	183.4	135.2	243.8	99.0	0.258	0.111	0.075	0.025	1.085	2.061	-0.356	3.142	2.60E-03	0.374	0.999	0.999	9.01E-04	3.50E-03	
600S137-68-DAM-2	$\delta_B$	239.6	162.6	96.7	73.5	0.146	0.110	0.029	0.021	0.869	1.123	-2.304	3.142	7.05E-04	-0.220	0.999	0.999	1.30E-03	4.30E-03
	$\delta_C$	166.6	84.8	609.3	69.7	0.074	0.041	0.023	0.020	-0.839	1.601	3.070	-2.107	6.05E-04	-0.189	0.997	0.996	1.10E-03	3.90E-03
	$\phi$	256.4	134.6	69.4	44.4	0.095	0.071	0.024	0.012	0.724	1.142	-0.875	-0.825	-2.80E-03	0.691	0.991	0.990	5.50E-03	8.60E-03
	$\delta_w$	96.8	128.4	72.5	62.2	0.020	0.012	0.009	0.005	3.102	-3.103	2.546	3.140	9.59E-05	-0.033	0.953	0.946	8.21E-04	3.30E-03
	$\delta_{FE}$	258.4	87.9	122.4	72.0	0.147	0.068	0.061	0.041	-2.119	2.874	-3.142	3.142	1.60E-03	-0.419	0.990	0.989	1.51E-02	1.40E-02
$\delta_{FW}$	144.5	110.5	192.5	98.0	0.355	0.241	0.232	0.124	0.820	1.426	-0.236	3.142	4.62E-04	0.216	0.997	0.996	3.50E-03	6.90E-03	
600S137-68-DAC-2	$\delta_B$	155.9	180.7	91.0	55.6	0.155	0.137	0.027	0.011	1.908	-0.609	3.142	2.914	6.08E-04	-0.177	0.993	0.992	1.70E-03	4.90E-03
	$\delta_C$	211.5	523.9	87.6	66.5	0.120	0.051	0.037	0.011	2.635	1.020	1.079	-0.838	1.90E-03	-0.547	1.000	1.000	2.05E-04	1.70E-03
	$\phi$	110.3	93.5	71.9	287.3	0.140	0.085	0.030	0.017	-0.076	1.374	2.512	0.403	2.53E-04	-0.459	0.993	0.992	2.50E-03	6.00E-03
	$\delta_w$	214.7	179.3	96.4	54.5	0.223	0.151	0.017	0.008	0.447	3.009	3.142	1.795	-2.20E-03	1.052	0.992	0.991	4.20E-03	7.70E-03
	$\delta_{FE}$	252.8	118.3	85.8	51.6	0.074	0.074	0.053	0.015	-2.041	-3.063	3.142	1.874	2.30E-03	-0.768	0.976	0.973	1.50E-02	1.44E-02
$\delta_{FW}$	205.1	148.6	105.4	90.8	0.224	0.198	0.103	0.026	0.558	1.046	1.607	3.142	-2.80E-03	1.424	0.998	0.998	2.90E-03	6.50E-03	
800S250-68-DFC-2	$\delta_B$	368.8	738.4	227.0	157.2	0.036	0.029	0.026	0.020	0.235	1.784	-3.142	3.142	-1.53E-05	0.012	0.973	0.972	1.17E-02	6.40E-03
	$\delta_C$	746.8	386.8	271.8	175.0	0.141	0.103	0.078	0.034	1.594	1.179	1.830	2.160	1.30E-03	-0.979	0.998	0.997	1.19E-02	6.40E-03
	$\phi$	206.9	181.6	242.7	735.7	0.040	0.032	0.030	0.020	-1.584	-0.648	-2.362	-1.642	-5.87E-05	-0.096	0.988	0.987	2.80E-03	3.10E-03
	$\delta_w$	333.6	798.0	254.0	216.2	0.137	0.137	0.137	0.077	-2.526	-1.412	-1.966	-0.556	-1.12E-05	0.798	0.972	0.971	2.35E-01	2.85E-02
	$\delta_{FE}$	646.7	484.3	295.4	96.6	0.348	0.222	0.096	0.007	0.791	3.003	3.141	3.142	3.09E-05	-0.689	0.993	0.993	5.95E-02	1.44E-02
$\delta_{FW}$	806.3	255.3	321.5	239.7	0.237	0.237	0.163	0.153	-1.482	-1.616	-3.142	0.778	2.88E-05	-0.782	0.994	0.993	9.11E-02	1.77E-02	
800S250-68-DFM-2	$\delta_B$	306.2	347.4	676.3	181.5	0.155	0.150	0.100	0.053	-0.574	3.142	-1.395	-1.641	-1.96E-04	0.150	0.991	0.991	2.80E-02	9.80E-03
	$\delta_C$	338.3	188.4	565.1	240.3	0.033	0.024	0.023	0.014	-2.716	1.144	1.213	-0.386	1.88E-04	-0.144	0.991	0.991	3.40E-03	3.40E-03
	$\phi$	756.5	343.4	182.9	123.7	0.057	0.026	0.017	0.011	1.707	-0.833	-2.176	0.834	-5.05E-05	-0.132	0.984	0.984	9.80E-03	5.80E-03
	$\delta_w$	780.2	260.4	314.4	219.7	0.115	0.113	0.109	0.046	-1.383	-1.764	-3.142	-0.382	6.16E-05	0.756	0.981	0.980	7.82E-02	1.65E-02
	$\delta_{FE}$	642.3	468.9	347.4	478.8	0.250	0.213	0.080	0.030	1.168	2.157	3.142	1.249	2.15E-04	-0.845	0.997	0.997	2.03E-02	8.40E-03
$\delta_{FW}$	749.7	273.2	341.0	223.8	0.175	0.175	0.160	0.056	-1.588	-1.113	-2.454	-0.199	2.89E-05	-0.823	0.992	0.992	6.27E-02	1.47E-02	
1200S250-97-DFC-1	$\delta_B$	797.4	499.8	273.8	159.9	0.157	0.076	0.072	0.032	-1.773	1.715	0.330	-1.329	5.06E-05	-0.040	0.996	0.996	2.62E-02	9.50E-03
	$\delta_C$	237.6	226.8	351.1	1188.1	0.157	0.141	0.091	0.015	2.916	-0.229	-0.652	3.029	-8.80E-04	0.687	0.987	0.987	3.03E-02	1.03E-02
	$\phi$	514.8	248.7	307.1	151.3	0.033	0.028	0.013	0.012	-1.147	0.660	-3.141	-1.412	-2.93E-04	0.201	0.980	0.979	6.20E-03	4.70E-03
	$\delta_w$	212.3	870.8	133.0	263.3	0.071	0.039	0.021	0.017	-0.125	2.194	-3.142	0.096	-4.43E-05	0.827	0.966	0.965	3.68E-02	1.13E-02
	$\delta_{FE}$	397.8	522.2	285.6	131.3	0.144	0.137	0.086	0.013	1.711	1.177	3.128	0.742	6.09E-04	0.084	0.993	0.993	2.93E-02	1.01E-02
$\delta_{FW}$	382.8	189.3	277.1	911.3	0.042	0.031	0.027	0.018	-2.213	1.902	-0.826	1.324	1.13E-05	0.335	0.838	0.831	7.96E-02	1.66E-02	
1200S250-97-DFM-1	$\delta_B$	275.7	478.8	576.9	287.9	0.42	0.40	0.39	0.38	-0.36	3.14	0.32	3.14	-3.66E-05	0.03	0.99	0.99	7.47E-02	1.60E-02
	$\delta_C$	224.6	763.9	442.6	196.7	0.12	0.12	0.11	0.06	-1.04	-2.28	0.81	1.45	-1.20E-03	0.92	1.00	1.00	3.16E-02	1.05E-02
	$\phi$	254.8	235.2	725.0	403.0	0.13	0.13	0.08	0.04	3.14	-0.64	-1.17	3.14	-2.08E-04	0.26	0.95	0.95	9.07E-02	1.77E-02
	$\delta_w$	207.3	286.3	649.4	143.7	0.04	0.04	0.03	0.02	2.33	0.05	-2.63	1.35	-1.21E-04	0.81	0.98	0.97	1.77E-02	7.80E-03
	$\delta_{FE}$	359.5	266.9	218.9	177.0	0.14	0.08	0.03	0.01	1.73	1.24	2.39	3.14	9.13E-04	0.20	0.98	0.98	6.73E-02	1.53E-02
$\delta_{FW}$	362.2	291.4	579.3	163.5	0.15	0.15	0.06	0.03	-2.04	-0.31	-3.14	0.92	5.98E-05	0.44	0.98	0.98	3.72E-02	1.13E-02	

## Welcome to the Cold-Formed Steel Imperfections Database!

Hosted by the Cold-Formed Steel Research Consortium

This database is a collection of initial geometric imperfection measurements in Cold-Formed Steel research. Designed by cold-formed steel enthusiasts at Virginia Tech, it is our hope that this database will be communally expanded and used by past, present, and future researchers.

Each set of measurements is provided as a text file in the form of an x-y-z point cloud. In order to maintain unity within the database, all point clouds should be provided with the origin located at the transverse center of the web points, on the outside face of the web, beginning at one end of a member. The figure below illustrates the origin location for a C-shaped cross-section.



The "Summary" tab summarizes all point clouds that are currently included in the database. This list should be updated each time a new measurement set is added. This summary includes information about each point cloud, including the primary researcher, supporting university, advising professor, measurement method and section information.

The "References" tab includes a list of supporting publications that are related to the point clouds included in the database. These publications are referenced by number in the "Summary" tab.

Figure A1: Database interface – “About”

Point Cloud	File Name	Publication Date	Primary Contact	Secondary Contact	Supporting University	Advising Professor	Measurement Method	Section Type	Nominal Web Height (mm)	Nominal Flange Width (mm)	Nominal Thickness (mm)	Length (mm)	Section Notes	Supporting Publications
1	362S137-68-GAC-2	11/18/13	L.E. McAnallen (lem421@vt.edu)	D.A. Padilla-Llano (dapadill@vt.edu)	Virginia Tech	C.D. Moen (cmoen@vt.edu)	Photogrammetry	C-shaped	92.1	34.9	1.73	2286	SSMA Section 362S137-68	[1]
2	362S137-68-DAM-2	11/18/13	L.E. McAnallen (lem421@vt.edu)	D.A. Padilla-Llano (dapadill@vt.edu)	Virginia Tech	C.D. Moen (cmoen@vt.edu)	Photogrammetry	C-shaped	92.1	34.9	1.73	610	SSMA Section 362S137-68	[1]
3	362S137-68-DAC-2	11/18/13	L.E. McAnallen (lem421@vt.edu)	D.A. Padilla-Llano (dapadill@vt.edu)	Virginia Tech	C.D. Moen (cmoen@vt.edu)	Photogrammetry	C-shaped	92.1	34.9	1.73	610	SSMA Section 362S137-68	[1]
4	362S162-54-LAM-2	11/18/13	L.E. McAnallen (lem421@vt.edu)	D.A. Padilla-Llano (dapadill@vt.edu)	Virginia Tech	C.D. Moen (cmoen@vt.edu)	Photogrammetry	C-shaped	92.1	41.3	1.37	305	SSMA Section 362S162-54	[1]
5	362S162-54-LAC-1	11/18/13	L.E. McAnallen (lem421@vt.edu)	D.A. Padilla-Llano (dapadill@vt.edu)	Virginia Tech	C.D. Moen (cmoen@vt.edu)	Photogrammetry	C-shaped	92.1	41.3	1.37	305	SSMA Section 362S162-54	[1]

Figure A2: Database interface – “Summary”